Research Square

Preprints are preliminary reports that have not undergone peer review.
They should not be considered conclusive, used to inform clinical practice,
or referenced by the media as validated information.

B cells modulate Alzheimer's disease-related pathology in a mouse model of Down syndrome

Dolev Michaelovich
Bar-Ilan University
Angel Moren Fiomi
Bar-Ilan University
Hadassah Rosenfeld
Bar-Ilan University
Jennifer Israel-Cohen
Bar-Ilan University
Eitan Okun
Eitan.okun@biu.ac.il

Bar-Ilan University

Research Article

Keywords: Down syndrome, Alzheimer's disease, Adaptive Immunity, Amyloid-beta, Immunization, B-cell Depletion

Posted Date: November 3rd, 2026

DOI: https://doi.org/10.21203/rs.3.rs-11401656/v1

License: This work is licensed under a Creative Commons Attribution 4.0 International License.
Read Full License

Additional Declarations: No competing interests reported.

Abstract

Background

Individuals with Down syndrome (DS) are at exceptionally high risk of developing early-onset Alzheimer's disease (AD) and exhibit age-associated cognitive decline and chronic immune dysregulation. Although adaptive immunity can exert both protective and detrimental effects in neurodegenerative disorders, its contribution to AD-related pathology in DS remains poorly understood.

Methods

We characterized amyloid pathology, behavioral performance, and adaptive immune alterations in aged Dp1Tyb mice, a mouse model of DS. We further evaluated the effects of B-cell depletion using anti-CD20 antibody and active immunization against murine amyloid-beta (mAβ). Statistical analyses included t-tests, analysis of variance (ANOVA), and linear mixed-effects models, as appropriate.

Results

Aged Dp1Tyb mice exhibited increased soluble hippocampal and cortical $mA\beta_{40,}$ reduced $mA\beta_{42/40}$ ratios, short- and long-term spatial memory impairments, altered exploratory behavior, and impaired motor performance. These phenotypes were accompanied by systemic adaptive immune dysregulation, characterized by reduced mature B-cell populations and increased T-cell representation across peripheral and central nervous system (CNS)-associated immune compartments. B-cell depletion in male mice reduced soluble $mA\beta_{40}$ levels and selectively improved short-term spatial memory while inducing tissue-dependent increases in $CD4^+$ and $CD8^+$ T-cell abundance. Active mAβ immunization in female mice reduced soluble $mA\beta_{40}$ levels, partially normalized hippocampal microglial morphology, and was associated with improved short-term spatial memory-related performance.

Conclusions

These findings support adaptive immunity as a modifiable component of AD-related pathology in DS. Notably, B-cell depletion and active mAβ immunization converged on reduced $mA\beta_{40}$ and favorable short-term memory-related outcomes despite distinct effects on adaptive immune and microglial phenotypes, suggesting that multiple immune pathways can influence AD-related outcomes in DS. These findings are limited to a preclinical mouse model, and the mechanisms underlying the observed effects require further investigation.

Background

Down syndrome (DS), caused by trisomy of human chromosome 21 (Hsa21) [1], is associated with widespread immune dysregulation and chronic inflammation [2–5], as well as a markedly increased risk of early-onset Alzheimer's disease (AD). The majority of individuals with DS develop dementia by approximately 60 years of age [6, 7].

Adaptive immunity is increasingly recognized as a modulator of aging and AD-related neurodegeneration. T cells have been detected in cerebrospinal fluid and AD-affected brain regions [8, 9]. B cells have been proposed to exert protective effects in AD, including through humoral responses involving amyloid-beta (Aβ)-reactive antibodies (Abs) that could facilitate amyloid clearance [10]. However, experimental manipulation of adaptive immunity can modify neurodegenerative pathology. B-cell depletion, commonly achieved using anti-CD20 Abs, is an established therapeutic strategy in autoimmune diseases, including multiple sclerosis and rheumatoid arthritis [11, 12]. In AD mouse models, B-cell deficiency or therapeutic B-cell depletion has been reported to reduce Aβ pathology, improve cognitive outcomes, and alter microglial states [13, 14]. Conversely, profound impairment of adaptive immunity can accelerate AD pathology [15], indicating that intact adaptive immune responses may also contribute to central nervous system (CNS) homeostasis. In addition, active Aβ immunization has been shown to promote Aβ clearance and engage microglial clearance mechanisms in patients with AD and experimental models [16–19]. Thus, adaptive immunity can exert protective or detrimental effects depending on the cellular and disease context and can modify interconnected features of AD pathology.

The widespread adaptive immune abnormalities in DS include reduced transitional, naïve, and switched-memory B-cell populations, together with altered humoral responses [2, 20–22]. T-cell abnormalities include reduced naïve T-cell populations, accompanied by a shift toward activated, memory, and more differentiated phenotypes [2, 23–25]. These alterations have been linked to changes in immune signaling, particularly heightened interferon signaling [5, 26, 27], as well as chronic immune activation [2, 4] and features of premature immunosenescence [28]. Consistent with broader adaptive immune dysregulation, Dp1Tyb mice, a model of DS, exhibit an age-associated reduction in ectopic lymphoid-like structures (ELS) in the dura mater, suggesting altered maintenance of adaptive immune niches at CNS borders [29]. Additionally, previous analyses of Dp1Tyb mice found no significant increase in brain $CD8^+$ T-cell numbers compared with WT controls, in contrast to amyloid-depositing AD mouse models [30].

However, whether and how adaptive immune dysregulation is functionally linked to AD-related pathology in DS remains poorly understood. Here, we investigated whether interventions targeting adaptive immunity, particularly B cells, can modify AD-related pathology in DS. For this purpose, we used aged Dp1Tyb mice, which carry a duplication of the *Lipi-Zbtb21* region of mouse chromosome 16 encompassing approximately 63% of the mouse orthologs of Hsa21 genes, including *APP* and *Dyrk1a* [31]. We first characterized Aβ pathology, behavioral phenotypes, and B- and T-cell populations across peripheral and CNS-associated immune compartments in aged Dp1Tyb mice. We then applied two complementary immune-modulating interventions: B-cell depletion using an anti-CD20 antibody and active DNA immunization against murine Aβ (mAβ), building on our previous demonstration that DNA-

based Aβ immunization can modulate glial homeostasis and cognition in Ts65Dn mice, a different DS mouse model [32]. Following each intervention, we evaluated Aβ pathology, microglial morphology, adaptive immune composition, and behavioral outcomes.

Our findings demonstrate that distinct manipulations of adaptive immunity improve selected AD-related outcomes and identify the adaptive immune system, particularly the B-cell compartment, as a modifiable contributor to AD-related pathology in the Dp1Tyb mouse model of DS.

Materials and methods

Animals

Male and female Dp1Tyb mice (provided by Dr. Frances Wiseman, UK Dementia Research Institute, London, UK) were used as a mouse model of DS. Dp1Tyb mice carry a duplication of the *Lipi-Zbtb21* region of mouse chromosome 16 (Mmu16), encompassing ~63% of the mouse orthologs of Hsa21 genes [31]. All mice were group-housed under specific pathogen-free conditions at the Bar-Ilan University animal facility at 22°C on a 12 h light/12 h dark cycle, with adlibitum access to food and water. Heterozygous Dp1Tyb males were crossed with C57BL/6JOlaHsd females (Harlan) to generate Dp1Tyb and wild-type (WT) littermates, with WT littermates serving as controls in all experiments. Mice were randomly assigned to experimental treatment groups within each genotype. Animal care, genotyping, and experimental procedures were approved by the appropriate animal ethics committee at Bar-Ilan University and were conducted in accordance with institutional guidelines. Environmental enrichment, including nesting materials and shelters, was provided in the home cages. The health and welfare of the mice were monitored daily by the animal facility staff. At experimental endpoints, mice were anesthetized with ketamine-xylazine (100 and 10 mg/kg, respectively) and transcardially perfused with ice-cold phosphate-buffered saline (PBS).

Brain protein extraction

Following perfusion, the cerebral cortex and hippocampus were separated, immediately frozen on dry ice, and stored at -80°C. Tissues were subjected to sequential extraction to obtain Radioimmunoprecipitation assay buffer (RIPA)-soluble and formic acid-extracted insoluble protein fractions for Aβ quantification. For the isolation of the soluble fraction of Aβ, tissues were mechanically homogenized in RIPA buffer (150 mM NaCl, 5 mM EDTA (pH 8), 50 mM Tris (pH 8), 1% Triton X-100, 0.5% sodium deoxycholate, 0.1% sodium dodecyl sulfate (SDS), dH_2O) with protease inhibitor cocktail (1:100, Cat# P2714, Sigma) and phosphatase inhibitor cocktail (1:100, Cat# 524625, Sigma), at 150 mg of tissue per ml of buffer, then incubated on ice for 30 min, followed by centrifugation at 17,000 × *g* for 2 h at 4°C. The supernatant, containing soluble Aβ, was removed and stored at -80°C. The remaining pellet, containing insoluble Aβ, was resuspended in 70% formic acid at 450 mg of tissue per ml of formic acid and incubated on ice for 30 min, followed by centrifugation under the same conditions as above. The formic acid supernatant was collected and neutralized with 1 M Tris pH 11 (20 times the volume of formic acid), then stored at -80°C. Total protein concentration was determined in mg/ml using a

bicinchoninic acid (BCA) assay at a dilution of 1:20 for soluble fractions, and 1:50 for insoluble fractions (Cat# 23225, Thermo Fisher). Aβ concentrations were normalized to total protein content and expressed as pg Aβ/mg total protein. Experimental protocol is shown in Fig. S1.

Murine Aβ measurements using a sandwich enzyme-linked immunosorbent assay(**sELISA**).

Assay protocol, development, calibration, antibody selection, and validation are described in Figs. S1-S3. Brain-derived Aβ was quantified using 96-well polystyrene microplates (Cat# 655061, Greiner), pre-coated with 50 µl of the appropriate capture Ab (Fig. S2a, b), diluted in carbonate**-**bicarbonate buffer (pH 9.6), and incubated overnight at 4°C. The plates were then washed four times with PBS containing 0.05% Tween (PBS-T), blocked for 1 h at room temperature (RT) with 2% BSA in PBS**-**T, and washed fourtimes with PBS**-**T. Subsequently, 50 µl of the appropriate dilution of soluble or insoluble protein homogenate was added to each well (Fig. S2c), and the plates were incubated for 2 h at RT. Then, the plates were washed five times with PBS-T, followed by the addition of 100 µl of the relevant detection Ab diluted in blocking solution (Fig. S2a, b). Samples were further incubated for 2 h at RT. Following a final wash (5 × PBS**-**T), 3, 3', 5, 5'**-**tetramethylbenzidine (TMB) substrate(Cat# 00-4201-56, eBioscience, Thermo Fisher) was added to initiate the colorimetric reaction. The reaction was stopped by adding 50 µl of 2 M H_2SO_4. Absorbance was measured at 450 nm using a spectrophotometer. Quantification was based on standard curves generated with known concentrations of recombinant murine $A\beta_{40}$ and $A\beta_{42}$ peptides (Fig. S2b, d).

Flow cytometry

Antibody details are provided **in Fig. S4a**. Single-cell suspensions were prepared from peripheral blood, spleen, dural meninges, superficial cervical lymph nodes (scLN), deep cervical lymph nodes (dcLN), and mesenteric lymph nodes (mLN). Blood was collected into tubes containing ethylenediaminetetraacetic acid (EDTA) (Cat# 450530, Greiner) and gently inverted to prevent coagulation. Red blood cells were lysed with Ammonium-Chloride-Potassium (ACK) buffer (Cat# A1049201, Gibco) for 5 min in the dark, followed by centrifugation at 300 × *g* for 5 min and washing with Roswell Park Memorial Institute (RPMI) 1640 medium (Cat# 01-100-1A, SARTORIUS). Samples were centrifuged again (300 × *g*, 5 min) and resuspended in PBS. Spleens were collected into cold RPMI and gently dissociated by mechanical disruption using the plunger of a sterile syringe on a 70 µm cell strainer. The cell suspension was washed twice with 2 ml of RPMI, then centrifuged at 300 × *g* for 8 min. Red blood cells were lysed with ACK lysis buffer for 5 min at RT in the dark, followed by centrifugation at 300 × *g* for 5 min. Cells were then washed with RPMI, centrifuged again (300 × *g*, 5 min), and resuspended in PBS. Dural meningeal tissue was digested for 15 min at 37°C with constant agitation using 0.5 ml of pre-warmed digestion buffer containing RPMI medium with 2% fetal bovine serum (FBS), 0.5 mg/ml collagenase VIII, and 0.05 mg/ml DNase I. The digested material was then passed through a cell strainer cap (Cat# 352235, Fisher Scientific), and enzymatic activity was neutralized with 1 ml of complete RPMI medium containing 10% FBS. Cells were centrifuged at 400 × *g* for 5 min and resuspended in PBS.**Lymph nodes were collected in ice-cold RPMI supplemented with 5% FBS. Each node was carefully dissected and then mechanically**

dissociated by gently triturating the tissue through a cell strainer cap in RPMI. Remaining tissue fragments on the strainer were washed twice with 1 ml of RPMI. Cell suspensions were centrifuged at 300 × *g* for 10 min and resuspended in PBS.Gating strategy is provided in Fig. S4b. For the ex vivo Aβ experiment,synthetic murine $A\beta_{1\text{-}42}$ (Cat# ab120959, Abcam) was prepared in 1% NH_4OH/water, diluted to 100 µM in PBS, and incubated at 4°C for 48 h to promote oligomerization. Splenocyte and scLN cultures were subsequently stimulated with 10 µg of oligomerized $mA\beta_{1\text{-}42}$ per sample. Cells were incubated for 24 h at 37°C in 5% CO_2 with either murine $A\beta_{1\text{-}42}$ or 1% NH_4OH/water for non-activated samples. Cells were cultured in RPMI supplemented with 10% FBS, 1% of 0.1 mM penicillin-streptomycin-nystatin, and 2 mM L-glutamine. Following incubation, cells were collected by centrifugation for subsequent staining. Gating strategy is provided in Fig. S5.**For all experiments and tissues, cell viability was determined by incubating cells with Ghost Dye diluted in PBS for 30 min at 4°C. To block nonspecific interactions, cells were treated with 5% normal rat serum (Cat# sc-45135, Santa Cruz) in PBS containing 1%** bovine serum albumin (**BSA) for 20 min at 4°C. Extracellular staining was then performed using fluorophore-conjugated monoclonal Abs diluted in FACS buffer (PBS with 1% BSA and 2 mM EDTA), supplemented with 50 µl of Brilliant Stain Buffer (Cat# 563794, BD Horizon) as needed to minimize fluorochrome-to-fluorochrome interactions**.Staining was performed for 20 min at 4°C, followed by washing and resuspension in 300 µl of FACS buffer prior to acquisition. All Abs were titrated prior to use. To ensure proper compensation and gating, single-stained, unstained, and fluorescence minus one (FMO) controls were included in each experiment. Data were recorded on a Cytek Aurora spectral flow cytometer. For each tissue, an equal number of live cells, normalized to the number of viable cells recovered from that tissue, was exported per sample and analyzed in FlowJo v10.10.0.

Immunohistochemistry and microglial morphology analysis

For microglial morphology assessment, one hemisphere from each Dp1Tyb and WT mouse brain was collected in 4% paraformaldehyde (PFA) following perfusion. Hemi-brains were transferred to 20% glucose overnight, then to 30% glucose overnight. Microtome sections (40 µm) containing the cortex and hippocampus were obtained. Sections were washed three times in PBS containing 0.1% Triton (5 min each), then blocked in a solution containing 10% normal horse serum (Cat# S-2000-20, Vector Laboratories), 2% BSA, and 1% glycine in PBS containing 0.1% Triton for 1 h at RT and incubated overnight with rabbit anti-Iba1 Ab (1:1000, Cat# ab178846, Abcam). After primary incubation, tissues were washed three times with 0.1% PBS-Triton for 5 min each, and incubated with secondary antibody (1:500, Alexa Fluor® 568 goat anti-rabbit, Cat# A-11011, Invitrogen) for 1 h at RT. Sections were then washed again (3 × 5 min in PBS-Triton 0.1%), followed by staining with nucleic acid dye (1:2000, Hoechst 33342, Thermo Fisher) for 10 min at RT. Finally, the sections were washed three times with PBS and mounted on positively charged slides. For each sample, two fields of view (medial cortex and CA1 region of the hippocampus) were acquired using a 40 × objective, a 1 × 1 image frame, and a z-stack spanning ~30 µm. Image analysis was conducted in Imaris using the Filament Tracer module.

B-cell depletion

B-cell depletion was achieved by intraperitoneal (i.p.) administration of an anti-mouse CD20 antibody (clone MB20-11, Cat# BE0356, BioXcell) or an isotype-matched control Ab (mouse IgG2c, Cat# BE0366, BioXcell). Mice received 150 µg of antibody in 200 µl of PBS by i.p. injection every 3 weeks for 4 months.

DNA vaccination

The AβCoreS pVAX1-based DNA vaccine was generated in this study, encoding the N-terminal fragment of murine Aβ ($Aβ_{1-11}$) fused to a Hepatitis B surface antigen (HBsAg) and core antigen (HBcAg). For large-scale vaccine production, the NucleoBond Xtra Maxi-prep EF kit was used (Cat# 740424, MACHEREY-NAGEL). DNA vaccination was administered with electroporation. Abdominal skin was shaved, cleaned with 70% ethanol, and allowed to dry before immunization. Mice were injected intramuscularly with 25 µg of DNA (50 µl) at three time points at 14-day intervals, followed by a fourth injection 3 months after the initial injection. Immediately after DNA injection, electroporation was applied at the injection site using a two-needle array electrode with 10-mm needles and an ECM830 electroporator. The electroporation configuration was one pulse of 450 V/cm, two repetitions, lasting 0.05 ms each at an interval of 0.125 s, followed by a second pulse of 110 V/cm, three repetitions lasting 10 ms each at an interval of 0.125 s.

Behavioral tests

Behavioral testing and analysis were performed by experimenters blinded to genotypes and treatment groups. Mouse behavior was recorded and analyzed using ANY-maze software.

Long-term spatial memory

Long-term spatial learning and memory were assessed using a variant of the modified Barnes maze (MBM) test [33], a hippocampus-dependent task in which mice learn to use spatial cues to locate an escape hole across repeated training trials. Mice were placed on a circular platform 122 cm in diameter with 40 randomly placed holes, one of which provided access to an escape chamber (target hole). Illumination above the apparatus was maintained at 1300 lux throughout the test to motivate the animals to search for the target hole, and four extra-maze visual cues were presented on the walls surrounding the MBM table for spatial memory assessment. Mice underwent either three 120 s trials per day or two trials per day with progressively reduced trial duration (from 45 s to 25 s), depending on the performance of the mice, to locate the target hole. Trials were separated by a 30 s intertrial interval. This procedure was repeated daily until test duration reached a plateau. Exploration trajectories were classified into six spatial search strategies - Direct, Corrected, Long Correction, Circling, Accidental Circling, and Random- using a convolutional neural network-based classifier previously developed and validated in our laboratory [34]. Strategy utilization was expressed as the percentage of trials assigned to each strategy. A cognitive score was calculated by weighting each strategy according to its previously established cognitive value (Direct = 1, Corrected = 0.773, Long Correction = 0.618, Circling = 0, Accidental Circling = 0.330, and Random = 0.109), with higher scores reflecting the use of more efficient spatial strategies. To quantify cumulative strategy utilization across training, the area under the curve of

the percentage use of each strategy across consecutive testing days was calculated using the trapezoidal rule.

Short-term memory

To assess short-term spatial recognition memory, mice were tested in the Y-maze forced-choice [35, 36], T-maze [37], and object location recognition (OLR) [38]tests. The Y- and T-maze forced-choice tests exploit mice's spontaneous tendency to explore a previously inaccessible arm, and the T-maze's distinct visual cues also enable assessment of spatial memory. The Y-maze consisted of three symmetrical arms (40 × 8 cm), with 20-cm-high walls. The T-maze consisted of 30 × 15 cm-high walls covered with different black-and-white patterns, with three extra-maze visual cues presented above and, on the walls, surrounding the apparatus. Both tests consisted of a training phase followed by a test phase. During training, one arm from each apparatus was blocked, and the mouse was allowed to explore the two open arms of the maze for 5 min. During the test phase, the previously blocked arm was opened, and the mouse could freely explore the maze for 3 min. In the OLR test, mice were placed in a 40 × 40 cm arena with two different objects. During an acquisition trial, the mice were allowed to explore their environment. Subsequently, the position of one object was changed.For all tests, novelty versus familiarity preferences were assessed by monitoring the number of entries and the time spent in each arm or object location. A preference index was calculated as the difference between the time spent in the novel and familiar arm or location, divided by the total time spent in both. The illumination above the apparatuses in all tests was maintained at 20 lux to minimize stress.

Exploratory behavior and anxiety assessment

Exploratory activity and anxiety-like behavior were assessed using the open field arena (OFA)task [39], which measures spontaneous exploration of the center and peripheral areas of an unfamiliar arena. Mouse exploration in a 40 × 40 cm arena was recorded, with the outer 8 cm defined as the periphery and the inner 24 × 24 cm as the center. Mice were allowed to freely explore the arena for 5 min under 20-lux illumination.

Motor coordination

Motorabilities were assessed using a modified beam-walking test protocol [40, 41]. Briefly, mice were trained to cross a set of beams to reach a secure enclosed platform. Traversal latency, distance traveled, and movement speed were quantified as each mouse crossed square and cylindrical beams toward a 20 × 20 × 20 cm black cube located at the end. The apparatus was positioned 50 cm above the ground and set at a slight angle to encourage the mice to enter the target box. Each beam was 100 cm in length, and analyses were conducted only on the middle 80 cm, defined by marking 10 cm from both the start and end of each beam. Illumination above the apparatus was maintained at 1300 lux throughout the test to further motivate the animals. On the first day, mice were placed in the target box for a 60 s habituation period. Subsequently, all mice were tested on three square beams of decreasing width (28, 12, and 7

mm), performing three 60 s trials on each beam. On the following day, the beams were replaced with circular ones measuring 15, 20, and 30 mm in diameter.

Nesting behavior

To assess nesting behavior, mice were transferred into individual testing cages containing 1.8 g of nesting material. Nests were documented after 48 h, 96 h, or 120 h, depending on the performance of the mice. Nest-building performance was quantified as the mass of unshredded nesting material remaining at the predefined endpoint [42].

Statistics

Statistical tests were selected according to the experimental design. Comparisons were performed using Student's *t*-test, the Mann-Whitney test, two-way analysis of variance (ANOVA), or two-way repeated-measures ANOVA, as appropriate. Tukey's or Šídák's multiple-comparisons tests were applied for post hoc analyses, where appropriate. Three-way ANOVA or three-way repeated-measures ANOVA was used for experiments involving three factors and was performed in R (R Core Team). Where appropriate, linear mixed-effects models were fitted, with fixed effects and interactions evaluated using Type III ANOVA with the Satterthwaite approximation for degrees of freedom. Post hoc comparisons were performed using estimated marginal means with Benjamini-Hochberg false discovery rate (FDR) correction for multiple testing. Normality was assessed using the Shapiro-Wilk test. Where indicated, data were $\log_{10}$-transformed before statistical analysis. One-tailed tests were used for predefined directional comparisons. Outliers were identified and exluded using the robust regression and outlier removal (ROUT) method (Q = 1%) or, for grouped datasets, Tukey's fences (1.5 × interquartile range (IQR)). Data are presented as mean ± standard deviation (SD). Sample sizes were estimated a priori using G*Power (effect size = 0.8; α = 0.05). Statistical significance was defined as $p < 0.05$, $p < 0.01$, $p < 0.001$, and $p < 0.0001$. Unless otherwise indicated, analyses were performed using GraphPad Prism version 8.4.2 for Windows. The individual mouse was considered the experimental unit for all in vivo analyses.

Schematic illustrations in Figs. 4-6 were generated using OpenAI ChatGPT and reviewed by the authors.

Results

Aged Dp1Tyb mice exhibit increased soluble mAβ_{40} and reduced A$\beta_{42/40}$ ratios.

To characterize amyloid pathology, soluble and insoluble mAβ_{40} and mAβ_{42} were quantified in the hippocampus and cortex of 10-15-month-old male and female Dp1Tyb and WT mice using an in-house sELISA protocol (Fig. S1). Assay characterization, including capture and detection antibody combinations, epitopes, recombinant Aβ_{40} and Aβ_{42} standard curves, assay controls, and cross-reactivity assessment, is provided in Figs. S2, S3. Because no significant sex-dependent differences were detected in this cohort (Fig. S6), data from male and female mice were pooled for subsequent

analyses. In the hippocampus, soluble mAβ_{40} was significantly increased in Dp1Tyb mice compared with WT littermate controls (Fig. 1a, $p < 0.05$), whereas soluble mAβ_{42} did not differ significantly between genotypes (Fig. 1b). The insoluble hippocampal mA$\beta_{42/40}$ ratiowas significantly reduced in Dp1Tyb mice (Fig. 1c, $p < 0.05$), indicating an altered relative distribution of the two Aβ species. Insoluble hippocampal mAβ_{40} and mAβ_{42} levels were positively correlated in both genotypes, with a stronger association in Dp1Tyb mice (WT: $p < 0.05$, $R^2 = 0.32$; Dp1Tyb: $p < 0.0001$, $R^2 = 0.87$; Fig. 1d). No significant genotype difference was detected in the soluble hippocampal mA$\beta_{42/40}$ ratio (Fig. S7a), and soluble mAβ_{40} and mAβ_{42} did not show a significant association in either genotype (Fig. S7b). Likewise, when insoluble hippocampal mAβ_{40} and mAβ_{42} levels were examined separately, no significant genotype differences were detected (Fig. S7c, d). A similar alteration in Aβ composition was observed in the cortex. Soluble cortical mAβ_{40} levels were significantly increased in Dp1Tyb mice relative to WT controls (Fig. 1e, $p < 0.001$), whereas soluble mAβ_{42} levels did not differ significantly between genotypes (Fig. 1f). Both soluble and insoluble cortical mA$\beta_{42/40}$ ratios were significantly reduced in Dp1Tyb mice (Fig. 1g, h, $p < 0.01$ and $p < 0.05$, respectively). Insoluble cortical mAβ_{40} and mAβ_{42} levels were significantly positively correlated in Dp1Tyb mice but not in WT controls (Fig. 1i; Dp1Tyb: $p < 0.0001$, $R^2 = 0.84$). However, the individual insoluble cortical mAβ_{40} and mAβ_{42} levels did not differ significantly between genotypes (Fig. S7e, f), and no significant relationship was observed between the soluble cortical mAβ species in either genotype (Fig. S7g).

Aged male Dp1Tyb mice exhibit impairments across multiple functional domains.

We next assessed behavioral performance across multiple functional domains.In the MBM test, Dp1Tyb mice showed a non-significant trend toward longer escape latency and a lower success rate compared with WT mice (Fig. 2a, b).Analysis of spatial navigation strategies [34] showed that WT mice progressively increased their use of efficient, goal-directed strategies across training, whereas Dp1Tyb mice showed greater persistence of less efficient search strategies (Fig. 2c, d; complementary MBM measures are presented in Fig. S8a-f).

Short-term memory was subsequently evaluated using a Y-maze forced-choice test. Dp1Tyb mice showed a significantly longer latency to first enter the newly accessible arm than WT controls (Fig. 2e, $p < 0.05$; Fig. S8g), consistent with impaired short-term spatial novelty preference. Exploratory and anxiety-like behavior were next assessed in the OFA test. Dp1Tyb mice spent more time in the peripheral and corner regions and less time in the center than WT mice (Fig. 2f; genotype × time interaction, $p < 0.0001$; Fig. S8h-j), consistent with increased anxiety-like behavior. No significant genotype differences were detected in overall locomotor activity (Fig. S8k-l). Finally, motor coordination was evaluated using the beam-walking test. Dp1Tyb mice required more time to traverse the beams than WT controls (Fig. 2g; genotype × beam-level interaction, $p < 0.05$). Consistently, Dp1Tyb mice traveled a longer distance and moved at a lower speed during the task (Fig. S8m-q), further supporting impaired motor performance.

Adaptive immune cell composition is altered in aged Dp1Tyb mice.

Having characterized the molecular and behavioral phenotypes of aged Dp1Tyb mice, we next examined adaptive immune-cell composition. Immune-cell populations were characterized by flow cytometry in blood, meninges, spleen, scLN, dcLN, and mLN. Total B-cell representation was reduced in the blood, meninges, scLN, dcLN, mLN, and spleen of aged Dp1Tyb mice, accompanied by broad reductions in B2 cells and specifically in follicular (FO) B cells (Fig. 3). In contrast, $CD3^+$ T cells were increased in the blood, meninges, dcLN, spleen and mLN, while $CD4^+$ T cells were increased in the scLN, dcLN, mLN, and spleen (Fig. 3). This recurring cellular pattern is consistent with the systemic adaptive immune dysregulation associated with DS [3, 29]

B-cell depletion remodels T-cell abundance, reduces mAβ_{40} levels, and improves short-term memory in aged Dp1Tyb mice.

Given the prominent B-cell alterations observed in aged Dp1Tyb mice compared with controls, we examined the consequences of sustained B-cell depletion. As B cells contribute to the regulation of T-cell homeostasis and function [43, 44], we also examined whether B-cell depletion altered the T-cell compartment. Aged male Dp1Tyb and WT mice received an anti-CD20 B-cell-depleting antibody or isotype control every three weeks for four months (Fig. 4a). Flow cytometric analysis confirmed efficient B-cell depletion (Fig. 4b). Quantification across tissues demonstrated a robust treatment effect on B-cell numbers, with marked depletion in the blood, meninges, scLN, mLN, and spleen in both genotypes (Fig. 4c, $p < 0.001$).

Notably, B-cell depletion was accompanied by a tissue-dependent increase in T-cell abundance. $CD4^+$ T-cell numbers increased in the blood, scLN, and mLN, whereas the splenic increase was significant only in WT mice, with a non-significant trend in Dp1Tyb mice (Fig. 4d). Similarly, $CD8^+$ T-cell numbers increased in the blood and scLN, and in WT mice in the mLN and spleen, with a non-significant trend toward increased levels in Dp1Tyb mice in the spleen (Fig. 4e, $p = 0.055$). Neither $CD4^+$ nor $CD8^+$ T-cell numbers were significantly altered in the meninges. Consistent with these changes, total $CD3^+$ T-cell numbers increased in the blood, scLN, mLN, and spleen (Fig. S9a), whereas $CD4^-$ $CD8^-$ T-cell increases were restricted to the spleen (Fig. S9b). Plasma-cell changes were more limited, with increased numbers in the scLN of both genotypes and in the spleen of B-cell-depleted Dp1Tyb mice (Fig. S9c). These findings support the context-dependent interplay between B- and T-cell compartments.

We next examined whether B-cell depletion altered behavioral outcomes in Dp1Tyb mice. In the Y-maze forced-choice task, B-cell depletion significantly reduced the novel-to-familiar arm latency ratio, consistent with improved short-term memory (Fig. 4f). Additional Y-maze measures revealed treatment- and genotype-dependent effects on latency to familiar-arm entry and center occupancy in both Dp1Tyb and WT mice (Fig. S10a, b). In the OLR task, B-cell depletion increased entries into the novel-object location zone in both genotypes (Fig. 4g), with a corresponding reduction in exploration of the previous object location (Fig. S10c, d). In contrast, anxiety-like behavior in the OFA task remained predominantly genotype-dependent (Fig. S10e-g). Similarly, reduced nesting behavior (Fig. S10h) and impaired motor performance (Fig. S10i-n) were not rescued by B-cell depletion. These findings indicate that B-cell

depletion selectively modifies short-term spatial-memory-related performance, with evidence of benefit in Dp1Tyb mice.

B-cell depletion also significantly reduced soluble hippocampal mAβ_{40} across genotypes (Fig. 4h; treatment effect, $p < 0.05$). A similar reduction was observed as a non-significant trend in insoluble hippocampal mAβ_{40} (Fig. S10o).

Microglial morphology parameters remained largely unchanged in both the hippocampus and cortex (Fig. S11), indicating that the observed cognitive and biochemical changes were not accompanied by detectable changes in the measured microglial morphology parameters.

Female Dp1Tyb mice exhibit multi-domain behavioral impairments.

Before evaluating active mAβ immunization, we characterized the baseline behavioral phenotype of middle-aged (5-7-month-old) female Dp1Tyb mice. Immunization was initiated at 9-12 months, with post-immunization behavioral testing performed at 10-13 months and biochemical analyses at 13-15 months (Fig. 5a). During MBM acquisition, escape latency decreased across training days in both genotypes, whereas Dp1Tyb females showed poorer overall performance than WT controls (Fig. 5b). Dp1Tyb mice showed a significantly lower success rate and lower cognitive scores, reflecting reduced use of efficient spatial search strategies (Fig. 5c, d, respectively). Search-strategy analysis further demonstrated greater reliance on less efficient strategies in Dp1Tyb mice relative to WT mice (Fig. 5e), and a lower overall contribution of goal-directed search strategies (Fig. 5f). Additional MBM measures and representative trajectories are shown in Fig. S12a-g. In the forced-choice Y-maze, female Dp1Tyb mice showed reduced novel-arm preference, consistent with impaired short-term spatial memory (Fig. 5g; Fig. S12h-k). In the OFA, female Dp1Tyb mice displayed increased peripheral and corner activity, reduced center activity, greater distance traveled, and higher average speed, consistent with hyperactivity (Fig. 5h-j; Fig. S12l-o). Female Dp1Tyb mice also showed impaired nest-building behavior, reflected by greater residual unshredded nesting material (Fig. 5k), and impaired motor coordination, requiring more time and moving more slowly across the beams (Fig. 5l; Fig. S12p-t). Thus, middle-aged female Dp1Tyb mice exhibited behavioral abnormalities overlapping those observed in aged males, including spatial-memory and motor deficits, together with prominent hyperactivity and impaired nesting behavior.

Anti-mAβ immunization partially restores microglial homeostasis, **improves short-term memory and reduces mAβ_{40} pathology**.

Having established the baseline behavioral phenotype of female Dp1Tyb mice, we next examined the behavioral, pathological, and immunological effects of active mAβ immunization (Fig. 6a). Vaccination significantly reduced soluble and insoluble mAβ_{40} in the hippocampus and cortex across genotypes, with a greater reduction in Dp1Tyb mice (Fig. 6b; Fig. S13a-c). To determine whether vaccination elicited a mAβ-responsive adaptive immune response, we assessed lymphocyte activation following ex vivo stimulation with oligomeric mAβ. Vaccination induced tissue- and cell type-dependent changes in surface CD69 expression. In the spleen, increased CD69 expression was observed across all examined

populations, with the strongest response in plasma cells, whereas the scLN showed prominent plasma cell and $CD4^-$ $CD8^-$ T-cell responses accompanied by reduced CD69 levels in B cells, suggesting that immunization elicited a broad, compartment-specific adaptive immune response in aged mice (Fig. 6c). Next, short-term spatial memory was assessed using the T-maze test. Vaccinated Dp1Tyb mice showed a significantly greater novel-arm preference during the first 30 s of the test (Fig. 6d), accompanied by increased entries into the novel arm and a lower preference index for the familiar arm (Fig. S13d, e), supporting a vaccination-associated improvement of short-term spatial memory. In the OFA, behavioral responses differed between vaccinated Dp1Tyb and WT mice, with vaccinated Dp1Tyb mice showing fewer peripheral entries and more center entries (Fig. 6e; Fig. S13f), without significant differences in overall locomotor activity (Fig. S13g, h). In addition, mAβ immunization did not rescue nesting behavior or motor deficits (Fig. S13i-o), indicating that its behavioral effects were restricted to specific functional domains.

Finally, we examined whether mAβ immunization altered microglial morphology by quantifying features reflecting morphology and process complexity (Fig. 6f). In the hippocampus, naïve Dp1Tyb mice exhibited a more complex microglial morphology than WT controls, characterized by increased filament area, filament length, and branching. Vaccination, however, reduced these morphological measures in Dp1Tyb mice toward WT levels, consistent with a partial normalization of hippocampal microglial morphology (Fig. 6g-h; Fig. S14a-c). In contrast, cortical microglia did not show significant morphological differences between genotypes or vaccination groups (Fig. S14d-i). Thus, the effect of mAβ immunization on microglial morphology was predominantly observed in the hippocampus rather than uniformly across brain regions.

Discussion

In this study, we identified adaptive immunity, particularly the B-cell compartment, as a modifiable component of AD-related pathology in DS. Aged male and female Dp1Tyb mice showed increased hippocampal and cortical soluble $mA\beta_{40}$ and reduced insoluble hippocampal and soluble and insoluble cortical $mA\beta_{42/40}$ ratios (Fig. 1). Separate behavioral findings showed that aged male Dp1Tyb mice exhibited altered spatial-search behavior, short- and long-term memory impairments, anxiety-like behavior, and impaired motor performance (Fig. 2), whereas middle-aged females showed additional spatial-memory, nesting and hyperactivity abnormalities (Fig. 5). These changes were accompanied by a systemic shift in adaptive immunity in aged male and female Dp1Tyb mice, with reduced B-cell representation, particularly B2 and FO B cells, and increased $CD3^+$ and $CD4^+$ T-cell representation across peripheral and CNS-associated compartments (Fig. 3). Notably, the two mechanistically distinct immune interventions converged on selected disease-relevant outcomes. B-cell depletion in male mice reduced soluble hippocampal $mA\beta_{40}$, improved short-term-memory-related performance, and increased $CD4^+$ and $CD8^+$ T-cell abundance in a tissue-dependent manner (Fig. 4). Active mAβ immunization in female mice reduced soluble $mA\beta_{40}$, improved short-term memory and anxiety-related performance, and partially normalized hippocampal microglial morphology (Fig. 6). These findings suggest that adaptive

immunity in DS is not simply globally impaired but is remodeled in ways associated with, and experimentally linked to AD-related phenotypes.

The absence of overt amyloid plaques in Dp1Tyb mice [31] does not preclude the presence of AD-relevant pathology. Using the optimized sELISA, we identified a distinct amyloid phenotype characterized by increased soluble $mA\beta_{40}$ in the hippocampus and cortex and reduced $A\beta_{42/40}$ ratios in aged Dp1Tyb mice (Fig. 1). The predominance of soluble $mA\beta_{40}$ rather than $mA\beta_{42}$ is compatible with a non-plaque amyloid phenotype, given the greater aggregation propensity of $A\beta_{42}$ and its stronger association with fibrillary amyloid deposition [45, 46]. The coexistence of Aβ dysregulation and multi-domain functional impairment (Fig. 2) in the absence of overt plaque pathology supports using Dp1Tyb mice for investigating pre-plaque AD-related processes in DS.

The adaptive immune alterations observed in aged Dp1Tyb mice (Fig. 3) closely resemble the immune dysregulation described in individuals with DS [2, 3, 5]. Total B-cell, B2-, and FO B-cell representation was reduced across peripheral and CNS-associated compartments, whereas $CD3^+$ and $CD4^+$ T-cell representation was increased in multiple tissues. A similar imbalance has been described in individuals with DS, where contraction of the B-cell compartment coexists with chronic activation and phenotypic remodeling of $CD4^+$ T-cell populations [25]. Thus, rather than representing an isolated B-cell defect, our findings support broader adaptive immune remodeling involving opposing changes in B- and T-cell compartments across multiple tissues. The extension of these changes to the meninges was consistent with our previous observation of reduced numbers and complexity of dural ELS in aged Dp1Tyb mice [29], suggesting that DS-associated adaptive immune dysregulation also affects organized immune niches at the brain-immune interface.

Previous studies have shown that adaptive immune depletion can have divergent effects on AD pathology, emphasizing the importance of immune-cell context [13, 15]. Our findings extend this complexity to the Dp1Tyb model of DS. Despite the reduced B-cell compartment in Dp1Tyb mice (Fig. 3), further B-cell depletion (Fig. 4b, c) was associated with reduced hippocampal $mA\beta_{40}$ and improved short-term memory performance (Fig. 4f-h). This apparent paradox suggests that B-cell abundance alone may not determine their contribution to AD-related pathology, and that the identity and functional state of the remaining B cells may be particularly important.

One potential candidate is the age-associated B-cell (ABC) compartment. ABCs accumulate during aging and chronic inflammatory conditions and can exhibit enhanced antigen-presenting, inflammatory, and autoreactive properties [47–49]. Importantly, individuals with DS show enrichment of $CD11c^+$ T-bet^{high} $CD21^{low}$ B cells with features overlapping ABCs despite an overall contraction of the B-cell compartment [25]. Activated B-cell populations have also been implicated in microglial reactivity and amyloid-associated pathology [10, 13, 50]. Thus, the reduction of conventional B2 and FO populations observed in Dp1Tyb mice may coexist with relative preservation or enrichment of activated B-cell states, potentially shifting the functional balance of the residual B-cell compartment toward a more pathogenic phenotype. B-cell depletion treatment may therefore exert beneficial effects not simply by reducing B-cell

numbers, but by removing B-cell subsets that disproportionately contribute to inflammatory or amyloid-related pathology. Although our current flow-cytometry panel did not allow direct identification of ABC-like populations (Fig. S4), determining whether such populations are enriched in aged Dp1Tyb mice, particularly within CNS-associated immune compartments, will be important for resolving this possibility.

B-cell depletion also increased $CD4^+$ and $CD8^+$ T-cell abundance in a tissue- and genotype-dependent manner, extending its effects beyond B-cell removal to broader adaptive immune remodeling (Fig. 4d, e). These increases occurred in parallel with reduced $mA\beta_{40}$ and improved short-term memory-related performance (Fig. 4f-h), although this association does not establish that T-cell expansion mediated these effects. B cells can shape T-cell differentiation through antigen presentation, costimulatory signaling, and cytokine production [49, 51, 52], and B-cell depletion has been reported to shift T cells toward more naïve and less inflammatory states [53]. In aged mice, B-cell deficiency or anti-CD20 treatment reduced T-cell immunosenescence, particularly within the $CD4^+$ compartment, and was associated with improved health-span outcomes [53]. These findings raise the possibility that the increased T-cell populations observed here reflect functional remodeling rather than simply compensatory expansion. This distinction may be particularly relevant in AD, where T cells can exert both detrimental and protective effects, and profound adaptive immune deficiency can exacerbate amyloid pathology [15]. Determining the phenotype and antigen specificity of the expanded T-cells will be important for establishing whether they contribute to the beneficial effects of B-cell depletion.

The vaccination experiment provides a complementary view of this immune complexity (Fig. 6). Active mAβ immunization, which relies on adaptive immune recognition rather than elimination of a lymphocyte compartment, also reduced $mA\beta_{40}$ and improved short-term memory (Fig. 6b, d-e). Vaccination also induced compartment- and cell-type-dependent CD69 responses in plasma cells and selected T-cell populations after ex vivo mAβ stimulation (Fig. 6c), and partially restored hippocampal microglial morphology (Fig. 6g-h).

The apparent overlap between B-cell depletion and vaccination as beneficial interventions is not necessarily paradoxical, because B cells are heterogeneous and may exert both pathogenic and protective effects. In AD mouse models, activated B-cell populations displaying an inflammatory phenotype, including increased expression of IFN-γ and IL-6, have been associated with disease progression, while genetic B-cell deficiency or anti-CD20/B220-mediated B-cell depletion reduced Aβ pathology and ameliorated behavioral abnormalities [13]. Conversely, Aβ vaccination can induce anti-Aβ antibodies and reduce amyloid pathology [54], with antibody-mediated clearance proposed to occur through mechanisms including Fc receptor-dependent microglial phagocytosis [55] and peripheral sequestration of soluble Aβ [56]. Thus, B-cell depletion may be beneficial by removing activated disease-associated B-cell populations implicated in disease progression [13], whereas vaccination may instead harness an Aβ-specific humoral response to promote Aβ clearance.

The microglial findings further suggest that B-cell depletion and mAβ immunization may engage partly distinct biological pathways. B-cell depletion reduced mAβ_{40} and improved short-term memory without detectable changes in the microglial morphological parameters examined, whereas mAβ immunization shifted the increased filament area, length, and branching of Dp1Tyb hippocampal microglia toward WT levels. The absence of morphological changes following B-cell depletion, however, does not exclude functional microglial remodeling. B cells can directly modulate microglial activity through cytokines, immunoglobulins, and other soluble mediators [10, 49, 57]. In AD models, B-cell depletion has been shown to alter disease-associated microglial states while reducing Aβ pathology and improving behavioral outcomes [13], and ABCs have been shown to directly promote microglial reactivity, inflammatory states, and impaired microglial Aβ phagocytosis, further supporting a functional B-cell-microglia axis in AD [50]. Importantly, these interactions are likely context- and subset-dependent, as regulatory B-cell-derived signals can restrain neuro-inflammation, whereas other B-cell populations or their products may promote microglial dysfunction and impaired Aβ clearance [10, 13, 50, 57, 58]. Thus, the reduction in mAβ_{40} following B-cell depletion may involve changes in microglial phagocytosis, cytokine production, or transcriptional state that morphology alone does not capture. In contrast, Aβ immunization may more directly engage antibody-associated microglial clearance mechanisms, which could contribute to the morphological normalization observed following vaccination.

Limitations

Several limitations should be considered. Dp1Tyb mice carry murine *APP* and other triplicated mouse genes and do not develop the progressive amyloid plaque pathology characteristic of human AD in DS [31]. In addition, depletion and vaccination were examined in different sexes, restricting direct comparison between the interventions. Finally, some vaccination-related analyses included only vaccinated Dp1Tyb and WT mice, without corresponding unvaccinated controls, preventing vaccination-specific effects from being distinguished from genotype-dependent differences.

Conclusion

Overall, our data support a model in which adaptive immunity in DS, particularly the B-cell compartment, is remodeled rather than uniformly deficient. B and T cells may be protective and pathogenic, depending on cellular state, age, disease state, and tissue context. Both B-cell depletion and mAβ immunization reduced soluble mAβ_{40} and improved short-term memory-related performance, despite their distinct effects on T cells and microglia, suggesting that multiple immune pathways can modify early AD-related phenotypes in DS. Defining the B-cell states involved and their interactions with T cells, microglia, and Aβ may clarify the mechanisms linking adaptive immunity to AD-related pathology in DS and support the development of more selective immune-targeted interventions.

Abbreviations

ABC: Age-associated B cell

Ab: Antibody

AD: Alzheimer's disease

ANOVA: Analysis of variance

AUC: Area under the curve

Aβ: Amyloid-beta

BCA: Bicinchoninic acid

BSA: Bovine serum albumin

CE: Cell-type effect

CNS: Central nervous system

dcLN: Deep cervical lymph nodes

DS: Down syndrome

EDTA: Ethylenediaminetetraacetic acid

ELS: Ectopic lymphoid-like structures

FBS: Fetal bovine serum

FDR: False discovery rate

FMO: Fluorescence minus one

FO: Follicular

GE: Genotype effect

HBcAg: Hepatitis B core antigen

HBsAg: Hepatitis B surface antigen

i.p.: Intraperitoneal

IQR: Interquartile range

LE: Level effect

mAβ: Murine amyloid-beta

MBM: Modified Barnes maze

mLN: Mesenteric lymph nodes

MZ: Marginal zone

OFA: Open field arena

OLR: Object location recognition

PBS: Phosphate-buffered saline

PBS-T: Phosphate-buffered saline containing 0.05% Tween

PE: Phase effect

PFA: Paraformaldehyde

RIPA: Radioimmunoprecipitation assay

ROUT: Robust regression and outlier removal

RPMI: Roswell Park Memorial Institute

RT: Room temperature

scLN: Superficial cervical lymph nodes

SD: Standard deviation

SDS: Sodium dodecyl sulfate

sELISA: Sandwich enzyme-linked immunosorbent assay

TE: Treatment effect

TMB: 3,3',5,5'-Tetramethylbenzidine

WT: Wild type

Declarations

Ethics approval and consent to participate

All animal experiments were approved by the Bar-Ilan University Animal Care and Use Committee (approval no. BIU-BIU-IL-2503-113-1) and were conducted in accordance with institutional guidelines and applicable Israeli regulations for the care and use of laboratory animals. Consent to participate was not applicable, as the study did not involve human participants.

Consent for publication

Not applicable.

Availability of data and materials

The data supporting the findings of this study are available from the corresponding author upon reasonable request.

Competing interests

The authors declare they have no competing interests.

Funding

This study was funded by the Alzheimer's Association Grants SAGA23-1065793 and AARG-22-974362 and by the Bi-National Science Foundation (BSF) Grant 2021163.

Authors' Contributions

D.M. and E.O. designed the study and wrote the manuscript; D.M. conducted experiments and analyzed data; A.M.F., H.R.and J.I.C.contributed to experimental procedures and data analyses. All authors read and approved the final version.

Acknowledgements

Not applicable.

References

1. Antonarakis SE, Skotko BG, Rafii MS, Strydom A, Pape SE, Bianchi DW, Sherman SL, Reeves RH. Down syndrome. Nat Rev Dis Primers. 2020;6(1):9. https://doi.org/10.1038/s41572-019-0143-7
2. Illouz T, Biragyn A, Iulita MF, Flores-Aguilar L, Dierssen M, De Toma I, Antonarakis SE, Yu E, Herault Y, Potier MC, Botté A, Roper R, Sredni B, London J, Mobley W, Strydom A, Okun E. Immune dysregulation and the increased risk of complications and mortality following respiratory tract infections in adults with Down syndrome. Front Immunol. 2021;12:621440. https://doi.org/10.3389/fimmu.2021.621440
3. Ramba M, Bogunovic D. The immune system in Down syndrome: autoimmunity and severe infections. Immunol Rev. 2024;322(1):300-10. https://doi.org/10.1111/imr.13296

4. Sullivan KD, Evans D, Pandey A, Hraha TH, Smith KP, Markham N, Rachubinski AL, Wolter-Warmerdam K, Hickey F, Espinosa JM, Blumenthal T. Trisomy 21 causes changes in the circulating proteome indicative of chronic autoinflammation. Sci Rep. 2017;7(1):14818. https://doi.org/10.1038/s41598-017-13858-3
5. Waugh KA, Araya P, Pandey A, Jordan KR, Smith KP, Granrath RE, Khanal S, Butcher ET, Estrada BE, Rachubinski AL, McWilliams JA, Minter R, Dimasi T, Colvin KL, Baturin D, Pham AT, Galbraith MD, Bartsch KW, Yeager ME, Porter CC, Sullivan KD, Hsieh EW, Espinosa JM. Mass cytometry reveals global immune remodeling with multi-lineage hypersensitivity to type I interferon in Down syndrome. Cell Rep. 2019;29(7):1893-908.e4. https://doi.org/10.1016/j.celrep.2019.10.038
6. Maure-Blesa L, Carmona-Iragui M, Lott I, Head E, Wisniewski T, Rafii MS, Espinosa J, Flórez J, Mobley WC, Holland A, Strydom A, Zaman S, Fortea J. The history of Down syndrome-associated Alzheimer's disease; past, present, and future. Alzheimers Dement. 2025;21(6):e70158. https://doi.org/10.1002/alz.70158
7. Rafii MS, Schlachetzki Z, Barroeta I, Head E, Fortea J, Ances BM. Down syndrome and Alzheimer's disease: insights into biomarkers, clinical symptoms, and pathology. Lancet Neurol. 2025;24(9):753-62. https://doi.org/10.1016/S1474-4422(25)00237-6
8. Dulken BW, Buckley MT, Navarro Negredo P, Saligrama N, Cayrol R, Leeman DS, George BM, Boutet SC, Hebestreit K, Pluvinage JV, Wyss-Coray T, Weissman IL, Vogel H, Davis MM, Brunet A. Single-cell analysis reveals T cell infiltration in old neurogenic niches. Nature. 2019;571(7764):205-10. https://doi.org/10.1038/s41586-019-1362-5
9. Gate D, Saligrama N, Leventhal O, Yang AC, Unger MS, Middeldorp J, Chen K, Lehallier B, Channappa D, De Los Santos MB, McBride A, Pluvinage J, Elahi F, Tam GK, Kim Y, Greicius M, Wagner AD, Aigner L, Galasko DR, Davis MM, Wyss-Coray T. Clonally expanded CD8 T cells patrol the cerebrospinal fluid in Alzheimer's disease. Nature. 2020;577(7790):399-404. https://doi.org/10.1038/s41586-019-1895-7
10. Park JC, Noh J, Jang S, Kim KH, Choi H, Lee D, Kim J, Chung J, Lee DY, Lee Y, Lee H, Yoo DK, Lee AC, Byun MS, Yi D, Han SH, Kwon S, Mook-Jung I. Association of B cell profile and receptor repertoire with the progression of Alzheimer's disease. Cell Rep. 2022;40(12):111391. https://doi.org/10.1016/j.celrep.2022.111391
11. Edwards JC, Szczepanski L, Szechinski J, Filipowicz-Sosnowska A, Emery P, Close DR, Stevens RM, Shaw T. Efficacy of B-cell-targeted therapy with rituximab in patients with rheumatoid arthritis. N Engl J Med. 2004;350(25):2572-81. https://doi.org/10.1056/NEJMoa032534
12. Hauser SL, Waubant E, Arnold DL, Vollmer T, Antel J, Fox RJ, Bar-Or A, Panzara M, Sarkar N, Agarwal S, Langer-Gould A, Smith CH. B-cell depletion with rituximab in relapsing-remitting multiple sclerosis. N Engl J Med. 2008;358(7):676-88. https://doi.org/10.1056/NEJMoa0706383
13. Kim K, Wang X, Ragonnaud E, Bodogai M, Illouz T, DeLuca M, McDevitt RA, Gusev F, Okun E, Rogaev E, Biragyn A. Therapeutic B-cell depletion reverses progression of Alzheimer’s disease. Nat Commun. 2021;12(1):2185. https://doi.org/10.1038/s41467-021-22479-4

14. Späni C, Suter T, Derungs R, Ferretti MT, Welt T, Wirth F, Gericke C, Nitsch RM, Kulic L. Reduced β-amyloid pathology in an APP transgenic mouse model of Alzheimer's disease lacking functional B and T cells. Acta Neuropathol Commun. 2015;3:71. https://doi.org/10.1186/s40478-015-0251-x
15. Marsh SE, Abud EM, Lakatos A, Karimzadeh A, Yeung ST, Davtyan H, Fote GM, Lau L, Weinger JG, Lane TE, Inlay MA, Poon WW, Blurton-Jones M. The adaptive immune system restrains Alzheimer's disease pathogenesis by modulating microglial function. Proc Natl Acad Sci U S A. 2016;113(9):E1316-25. https://doi.org/10.1073/pnas.1525466113
16. Nicoll JAR, Buckland GR, Harrison CH, Page A, Harris S, Love S, Neal JW, Holmes C, Boche D. Persistent neuropathological effects 14 years following amyloid-β immunization in Alzheimer's disease. Brain. 2019;142(7):2113-26. https://doi.org/10.1093/brain/awz142
17. Rudan Njavro J, Vukicevic M, Fiorini E, Dinkel L, Müller SA, Berghofer A, Bordier C, Kozlov S, Halle A, Buschmann K, Capell A, Giudici C, Willem M, Feederle R, Lichtenthaler SF, Babolin C, Montanari P, Pfeifer A, Kosco-Vilbois M, Tahirovic S. Beneficial effect of ACI-24 vaccination on Aβ plaque pathology and microglial phenotypes in an amyloidosis mouse model. Cells. 2022;12(1):79. https://doi.org/10.3390/cells12010079
18. Sha S, Xing XN, Wang T, Li Y, Zhang RW, Shen XL, Cao YP, Qu L. DNA vaccines targeting amyloid-β oligomer ameliorate cognitive deficits of aged APP/PS1/tau triple-transgenic mouse models of Alzheimer's disease. Neural Regen Res. 2022;17(10):2305-10. https://doi.org/10.4103/1673-5374.337054
19. van Olst L, Simonton B, Edwards AJ, Forsyth AV, Boles J, Jamshidi P, Watson T, Shepard N, Krainc T, Argue BMR, Zhang Z, Kuruvilla J, Camp L, Li M, Xu H, Norman JL, Cahan J, Vassar R, Chen J, Castellani RJ, Nicoll JAR, Boche D, Gate D. Microglial mechanisms drive amyloid-β clearance in immunized patients with Alzheimer’s disease. Nat Med. 2025;31(5):1604-16. https://doi.org/10.1038/s41591-025-03574-1
20. Carsetti R, Valentini D, Marcellini V, Scarsella M, Marasco E, Giustini F, Bartuli A, Villani A, Ugazio AG. Reduced numbers of switched memory B cells with high terminal differentiation potential in Down syndrome. Eur J Immunol. 2015;45(3):903-14. https://doi.org/10.1002/eji.201445049
21. Seckin AN, Ozdemir H, Ceylan A, Artac H. Age-related alterations of the CD19 complex and memory B cells in children with Down syndrome. Clin Exp Med. 2018;18(1):125-31. https://doi.org/10.1007/s10238-017-0457-2
22. Valentini D, Marcellini V, Bianchi S, Villani A, Facchini M, Donatelli I, Castrucci MR, Marasco E, Farroni C, Carsetti R. Generation of switched memory B cells in response to vaccination in Down syndrome children and their siblings. Vaccine. 2015;33(48):6689-96. https://doi.org/10.1016/j.vaccine.2015.10.083
23. Araya P, Waugh KA, Sullivan KD, Núñez NG, Roselli E, Smith KP, Granrath RE, Rachubinski AL, Enriquez Estrada B, Butcher ET, Minter R, Tuttle KD, Bruno TC, Maccioni M, Espinosa JM. Trisomy 21 dysregulates T cell lineages toward an autoimmunity-prone state associated with interferon

hyperactivity. Proc Natl Acad Sci U S A. 2019;116(48):24231-41. https://doi.org/10.1073/pnas.1908129116

24. Lambert K, Moo KG, Arnett A, Goel G, Hu A, Flynn KJ, Speake C, Wiedeman AE, Gersuk VH, Linsley PS, Greenbaum CJ, Long SA, Partridge R, Buckner JH, Khor B. Deep immune phenotyping reveals similarities between aging, Down syndrome, and autoimmunity. Sci Transl Med. 2022;14(627):eabi4888. https://doi.org/10.1126/scitranslmed.abi4888
25. Malle L, Patel RS, Martin-Fernandez M, Stewart OJ, Philippot Q, Buta S, Richardson A, Barcessat V, Taft J, Bastard P, Samuels J, Mircher C, Rebillat A-S, Maillebouis L, Vilaire-Meunier M, Tuballes K, Rosenberg BR, Trachtman R, Casanova J-L, Notarangelo LD, Gnjatic S, Bush D, Bogunovic D. Autoimmunity in Down's syndrome via cytokines, CD4 T cells and CD11c+ B cells. Nature. 2023;615(7951):305-14. https://doi.org/10.1038/s41586-023-05736-y
26. Galbraith MD, Rachubinski AL, Smith KP, Araya P, Waugh KA, Enriquez-Estrada B, Worek K, Granrath RE, Kinning KT, Paul Eduthan N, Ludwig MP, Hsieh EWY, Sullivan KD, Espinosa JM. Multidimensional definition of the interferonopathy of Down syndrome and its response to JAK inhibition. Sci Adv. 2023;9(26):eadg6218. https://doi.org/10.1126/sciadv.adg6218
27. Sullivan KD, Lewis HC, Hill AA, Pandey A, Jackson LP, Cabral JM, Smith KP, Liggett LA, Gomez EB, Galbraith MD, DeGregori J, Espinosa JM. Trisomy 21 consistently activates the interferon response. eLife. 2016;5:e16220. https://doi.org/10.7554/eLife.16220
28. Marcovecchio GE, Ferrua F, Fontana E, Beretta S, Genua M, Bortolomai I, Conti A, Montin D, Cascarano MT, Bergante S, D'Oria V, Giamberti A, Amodio D, Cancrini C, Carotti A, Di Micco R, Merelli I, Bosticardo M, Villa A. Premature senescence and increased oxidative stress in the thymus of Down syndrome patients. Front Immunol. 2021;12:669893. https://doi.org/10.3389/fimmu.2021.669893
29. Fruitman Davidi A, Shirenova S, Michaelovich D, Benedetti G, Shtrasberg H, Shoval I, Hauschner H, Oz G, Vardy K, Hirsh T, Madar R, Stern EA, Rosenmann H, Biragyn A, Okun E. Dural ectopic lymphatic structures accumulate during aging and exhibit dysregulation in neurodegenerative diseases. Proc Natl Acad Sci U S A. 2025;122(33):e2425081122. https://doi.org/10.1073/pnas.2425081122
30. Wang X, Campbell B, Bodogai M, McDevitt RA, Patrikeev A, Gusev F, Ragonnaud E, Kumaraswami K, Shirenova S, Vardy K, Alameh M-G, Weissman D, Ishikawa-Ankerhold H, Okun E, Rogaev E, Biragyn A. CD8+ T cells exacerbate AD-like symptoms in mouse model of amyloidosis. Brain Behav Immun. 2024;122:444-55. https://doi.org/10.1016/j.bbi.2024.08.045
31. Lana-Elola E, Cater H, Watson-Scales S, Greenaway S, Müller-Winkler J, Gibbins D, Nemes M, Slender A, Hough T, Keskivali-Bond P, Scudamore CL, Herbert E, Banks GT, Mobbs H, Canonica T, Tosh J, Noy S, Llorian M, Nolan PM, Griffin JL, Good M, Simon M, Mallon AM, Wells S, Fisher EMC, Tybulewicz VLJ. Comprehensive phenotypic analysis of the Dp1Tyb mouse strain reveals a broad range of Down syndrome-related phenotypes. Dis Model Mech. 2021;14(10):dmm049157. https://doi.org/10.1242/dmm.049157

32. Illouz T, Madar R, Biragyn A, Okun E. Restoring microglial and astroglial homeostasis using DNA immunization in a Down syndrome mouse model. Brain Behav Immun. 2019;75:163-80. https://doi.org/10.1016/j.bbi.2018.10.004
33. Illouz T, Madar R, Okun E. A modified Barnes maze for an accurate assessment of spatial learning in mice. J Neurosci Methods. 2020;334:108579. https://doi.org/10.1016/j.jneumeth.2020.108579
34. Illouz T, Ascher LAB, Madar R, Okun E. Unbiased analysis of spatial learning strategies in a modified Barnes maze using convolutional neural networks. Sci Rep. 2024;14(1):15944. https://doi.org/10.1038/s41598-024-66855-8
35. Hadzibegovic S, Bontempi B, Nicole O. A novel Y-maze paradigm with enhanced sensitivity to subtle spatial recognition memory impairments in mice. BMC Methods. 2025;2(1):22. https://doi.org/10.1186/s44330-025-00043-6
36. Kraeuter AK, Guest PC, Sarnyai Z. The Y-maze for assessment of spatial working and reference memory in mice. Methods Mol Biol. 2019;1916:105-11. https://doi.org/10.1007/978-1-4939-8994-2_10
37. Deacon RMJ, Rawlins JNP. T-maze alternation in the rodent. Nat Protoc. 2006;1(1):7-12. https://doi.org/10.1038/nprot.2006.2
38. Denninger JK, Smith BM, Kirby ED. Novel object recognition and object location behavioral testing in mice on a budget. J Vis Exp. 2018(141). https://doi.org/10.3791/58593
39. Seibenhener ML, Wooten MC. Use of the open field maze to measure locomotor and anxiety-like behavior in mice. J Vis Exp. 2015(96):e52434. https://doi.org/10.3791/52434
40. Brooks SP, Dunnett SB. Tests to assess motor phenotype in mice: a user's guide. Nat Rev Neurosci. 2009;10(7):519-29. https://doi.org/10.1038/nrn2652
41. Carter RJ, Morton J, Dunnett SB. Motor coordination and balance in rodents. Curr Protoc Neurosci. 2001;Chapter 8:Unit 8.12. https://doi.org/10.1002/0471142301.ns0812s15
42. Deacon RM. Assessing nest building in mice. Nat Protoc. 2006;1(3):1117-9. https://doi.org/10.1038/nprot.2006.170
43. Tan D, Yin W, Guan F, Zeng W, Lee P, Candotti F, James LK, Saraiva Camara NO, Haeryfar SMM, Chen Y, Benlagha K, Shi LZ, Lei J, Gong Q, Liu Z, Liu C. B cell-T cell interplay in immune regulation: A focus on follicular regulatory T and regulatory B cell functions. Front Cell Dev Biol. 2022;10:991840. https://doi.org/10.3389/fcell.2022.991840
44. Van Meerhaeghe T, Néel A, Brouard S, Degauque N. Regulation of CD8 T cell by B-cells: A narrative review. Front Immunol. 2023;14:1125605. https://doi.org/10.3389/fimmu.2023.1125605
45. Jan A, Gokce O, Luthi-Carter R, Lashuel HA. The ratio of monomeric to aggregated forms of Abeta40 and Abeta42 is an important determinant of amyloid-beta aggregation, fibrillogenesis, and toxicity. J Biol Chem. 2008;283(42):28176-89. https://doi.org/10.1074/jbc.M803159200
46. Walker LC. Aβ plaques. Free Neuropathol. 2020;1:31. https://doi.org/10.17879/freeneuropathology-2020-3025

47. de Mol J, Kuiper J, Tsiantoulas D, Foks AC. The dynamics of B cell aging in health and disease. Front Immunol. 2021;12:733566. https://doi.org/10.3389/fimmu.2021.733566
48. Hao Y, O'Neill P, Naradikian MS, Scholz JL, Cancro MP. A B-cell subset uniquely responsive to innate stimuli accumulates in aged mice. Blood. 2011;118(5):1294-304. https://doi.org/10.1182/blood-2011-01-330530
49. Jain RW, Yong VW. B cells in central nervous system disease: diversity, locations and pathophysiology. Nat Rev Immunol. 2022;22(8):513-24. https://doi.org/10.1038/s41577-021-00652-6
50. Zhang J, Fang W, Liu H, Li R, Zhu Z, Wu X, Yao S, Fu Y, Li R, Chen W, Ye Q, Liu Q, Chen X. Bone marrow B lymphopoiesis accelerates early cerebral amyloid pathology. Signal Transduct Target Ther. 2025;10(1):312. https://doi.org/10.1038/s41392-025-02419-0
51. Molnarfi N, Schulze-Topphoff U, Weber MS, Patarroyo JC, Prod'homme T, Varrin-Doyer M, Shetty A, Linington C, Slavin AJ, Hidalgo J, Jenne DE, Wekerle H, Sobel RA, Bernard CC, Shlomchik MJ, Zamvil SS. MHC class II-dependent B cell APC function is required for induction of CNS autoimmunity independent of myelin-specific antibodies. J Exp Med. 2013;210(13):2921-37. https://doi.org/10.1084/jem.20130699
52. Sabatino JJ, Pröbstel A-K, Zamvil SS. B cells in autoimmune and neurodegenerative central nervous system diseases. Nat Rev Neurosci. 2019;20(12):728-45. https://doi.org/10.1038/s41583-019-0233-2
53. Khan S, Chakraborty M, Wu F, Chen N, Wang T, Chan YT, Sayad A, Kotlyar M, Alibhai FJ, Woo M, Li R-K, Husain M, Jurisica I, Gehring AJ, Ohashi PS, Furman D, Tsai S, Winer S, Winer DA. B cells drive CD4 T cell immunosenescence and age-associated health decline. Sci Immunol. 2026;11(115):eadv7615. https://doi.org/10.1126/sciimmunol.adv7615
54. Schenk D, Barbour R, Dunn W, Gordon G, Grajeda H, Guido T, Hu K, Huang J, Johnson-Wood K, Khan K, Kholodenko D, Lee M, Liao Z, Lieberburg I, Motter R, Mutter L, Soriano F, Shopp G, Vasquez N, Vandevert C, Walker S, Wogulis M, Yednock T, Games D, Seubert P. Immunization with amyloid-beta attenuates Alzheimer-disease-like pathology in the PDAPP mouse. Nature. 1999;400(6740):173-7. https://doi.org/10.1038/22124
55. Bard F, Cannon C, Barbour R, Burke RL, Games D, Grajeda H, Guido T, Hu K, Huang J, Johnson-Wood K, Khan K, Kholodenko D, Lee M, Lieberburg I, Motter R, Nguyen M, Soriano F, Vasquez N, Weiss K, Welch B, Seubert P, Schenk D, Yednock T. Peripherally administered antibodies against amyloid beta-peptide enter the central nervous system and reduce pathology in a mouse model of Alzheimer disease. Nat Med. 2000;6(8):916-9. https://doi.org/10.1038/78682
56. DeMattos RB, Bales KR, Cummins DJ, Dodart JC, Paul SM, Holtzman DM. Peripheral anti-A beta antibody alters CNS and plasma A beta clearance and decreases brain A beta burden in a mouse model of Alzheimer's disease. Proc Natl Acad Sci U S A. 2001;98(15):8850-5. https://doi.org/10.1073/pnas.151261398

57. Geladaris A, Häusser-Kinzel S, Pretzsch R, Nissimov N, Lehmann-Horn K, Häusler D, Weber MS. IL-10-providing B cells govern pro-inflammatory activity of macrophages and microglia in CNS autoimmunity. Acta Neuropathol. 2023;145(4):461-77. https://doi.org/10.1007/s00401-023-02552-6

58. Feng W, Zhang Y, Ding S, Chen S, Wang T, Wang Z, Zou Y, Sheng C, Chen Y, Pang Y, Marshall C, Shi J, Nedergaard M, Li Q, Xiao M. B lymphocytes ameliorate Alzheimer's disease-like neuropathology via interleukin-35. Brain Behav Immun. 2023;108:16-31. https://doi.org/10.1016/j.bbi.2022.11.012

Figures

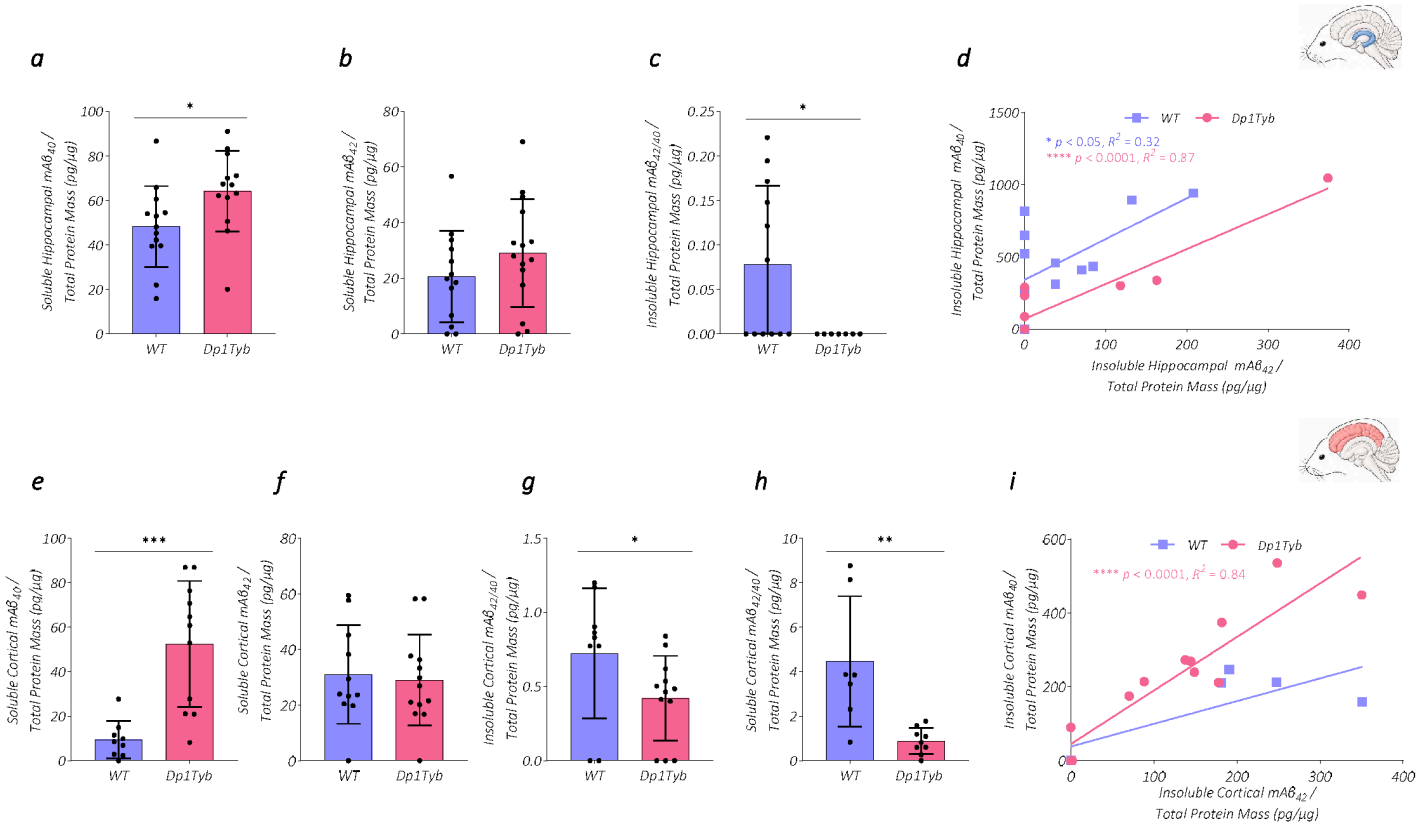


Figure 1

Aged Dp1Tyb mice exhibit increased soluble mAβ$_{40}$ and altered mAβ$_{42/40}$ ratios. (a) Soluble hippocampal mAβ$_{40}$ levels were significantly increased in Dp1Tyb mice compared with WT controls (p < 0.05; n = 13 per group). (b) Soluble hippocampal mAβ$_{42}$ levels did not differ significantly between genotypes (Dp1Tyb: n = 15; WT: n = 13). (c) The insoluble hippocampal mAβ$_{42/40}$ ratio was significantly reduced in Dp1Tyb mice compared with WT controls (p < 0.05; Dp1Tyb: n = 7; WT: n = 12). (d) Insoluble hippocampal mAβ$_{40}$ and mAβ$_{42}$ concentrations were significantly associated in both genotypes

(Dp1Tyb: $p < 0.0001$, $R^2 = 0.87$, n = 10; WT: $p < 0.05$, $R^2 = 0.32$, n = 12). (e) Soluble cortical $mA\beta_{40}$ levels were significantly increased in Dp1Tyb mice compared with WT controls ($p < 0.001$; Dp1Tyb: n = 11; WT: n = 9). (f) Soluble cortical $mA\beta_{42}$ levels did not differ significantly between genotypes (Dp1Tyb: n = 13; WT: n = 11). (g) The soluble cortical $mA\beta_{42/40}$ ratio was significantly reduced in Dp1Tyb mice compared with WT controls ($p < 0.01$; Dp1Tyb: n = 9; WT: n = 7). (h) Dp1Tyb mice showed a significantly reduced insoluble cortical $mA\beta_{42/40}$ ratio compared with WT controls ($p < 0.05$; Dp1Tyb: n = 12; WT: n = 9). (i) Insoluble cortical $mA\beta_{40}$ and $mA\beta_{42}$ concentrations were significantly positively associated in Dp1Tyb mice ($p < 0.0001$, $R^2 = 0.84$), whereas no significant association was detected in WT mice (Dp1Tyb: n = 13; WT: n = 6). Normality was assessed using the Shapiro-Wilk test. Between-genotype comparisons were performed using an unpaired Student's *t*-test or the Mann-Whitney test, as appropriate. Linear regression was used to assess relationships between $mA\beta_{40}$ and $mA\beta_{42}$ concentrations. Data are presented as mean ± SD. Each point represents an individual mouse. Statistical significance is denoted as * $p < 0.05$, ** $p < 0.01$, *** $p < 0.001$, and **** $p < 0.0001$.

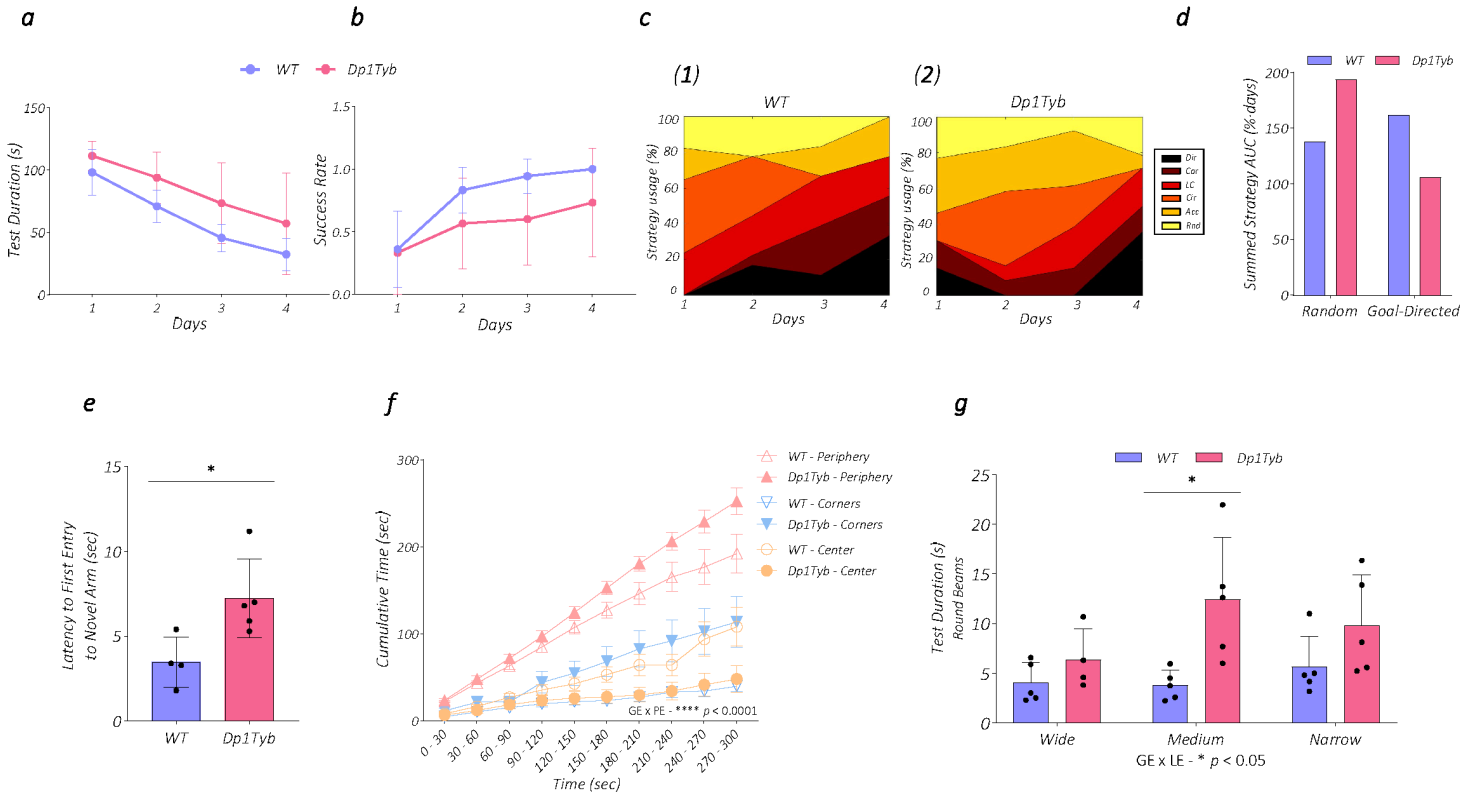


Figure 2

Aged male Dp1Tyb mice show deficits across long- and short-term memory, anxiety-related behavior, and motor coordination. (**a**-**d**) **MBM**. Long-term spatial learning was tested in aged male Dp1Tyb and WT mice (Dp1Tyb: n = 5; WT: n = 6). Dp1Tyb mice showed a non-significant trend toward (**a**) longer escape latency and (**b**) lower success rate. (**c**) Search-strategy composition across training is shown for WT ($\mathbf{c_1}$) and Dp1Tyb ($\mathbf{c_2}$) mice using six predefined strategies (Direct, Corrected, Long Correction, Circling, Accidental Circling, and Random). (**d**) The summed area under the curve (AUC) of random (Circling, Accidental Circling, and Random) and goal-directed (Direct, Corrected, and Long Correction) strategy use across training illustrates greater persistence of random search behavior in Dp1Tyb mice. Data were analyzed using two-way repeated-measures ANOVA with genotype and training day as factors, followed by Šídák's post hoc test where appropriate. (**e**) **Y-maze forced-choice**. Dp1Tyb mice showed a significantly longer latency to first enter the newly accessible arm than WT mice ($p < 0.05$; n = 6 per group). Normality was assessed using the Shapiro-Wilk test, followed by an unpaired t-test. (**f**) **OFA**. Cumulative time spent in the periphery, corners, and center is shown at 30 s intervals across the 5 min session. Dp1Tyb mice spent more time in peripheral and corner regions and less time in the center (GE × PE interaction, $p < 0.0001$; n = 6 per group). Two-way repeated-measures ANOVA with genotype and test phase as factors, followed by Šídák's post hoc test. (**g**) **Beam-walking**. Dp1Tyb mice required more time to traverse the beams in the beam-walking test (GE × LE interaction, $p < 0.05$). Post hoc analysis revealed a significant difference at the medium beam width ($p < 0.05$; Dp1Tyb: n = 5; WT: n = 6). Data were analyzed using two-way repeated-measures ANOVA with genotype and beam width as factors, followed by Šídák's post hoc test. Data are presented as mean ± SD. Each point represents an individual mouse. GE, genotype effect; LE, level effect; PE, phase effect. Statistical significance is denoted as * $p < 0.05$, ** $p < 0.01$, *** $p < 0.001$, and **** $p < 0.0001$.

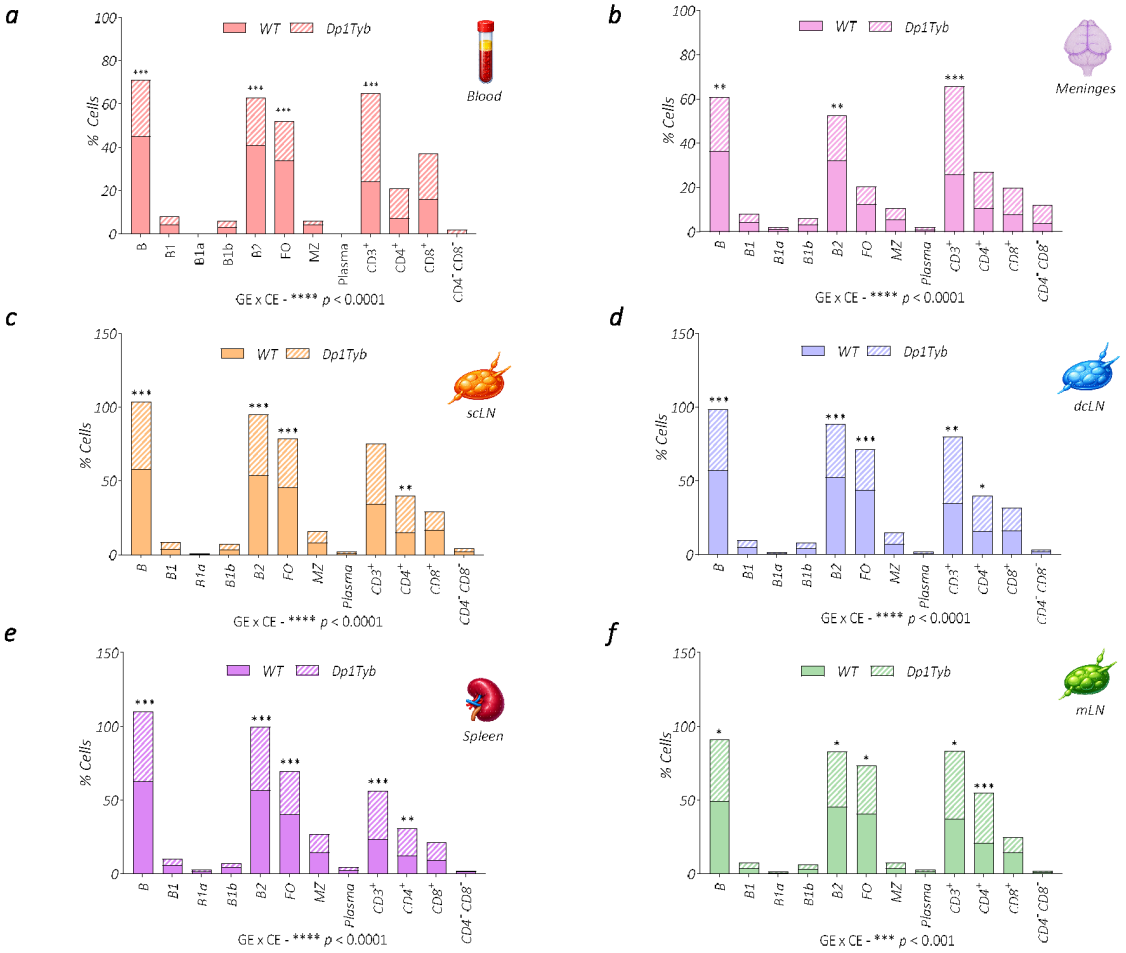


Figure 3

Aged Dp1Tyb mice exhibit systemic remodeling of adaptive immune cell composition. Adaptive immune cell populations were profiled by spectral flow cytometry in aged Dp1Tyb mice and WT controls using the antibodies and gating strategy described in Fig. S4. The relative representation of total B cells; B1, B1a, and B1b cells; B2 cells; FO B cells; marginal-zone (MZ) B cells; plasma cells; total $CD3^+$ T cells; $CD4^+$ T cells; $CD8^+$ T cells; and $CD4^-CD8^-$ T cells was assessed in each tissue. All changes below refer to relative cell representation in Dp1Tyb mice compared with WT controls. (a) Peripheral blood (n = 10 per group): reduced total B-cell, B2-, and FO B-cell representation, and increased $CD3^+$ T-cell representation ($p < 0.001$; GE × CE interaction, $p < 0.0001$). (b) Dural meninges (Dp1Tyb: n = 9; WT: n = 11): reduced total B-cell and B2-cell representation ($p < 0.01$), and increased $CD3^+$ T-cell representation ($p < 0.001$; GE × CE interaction, $p < 0.0001$). (c) The scLN (Dp1Tyb: n = 10; WT: n = 12): reduced B-cell populations, including B2 and FO B cells ($p < 0.001$), and increased $CD4^+$ T-cell representation ($p < 0.01$; GE × CE interaction, $p < 0.0001$). (d) The dcLN (Dp1Tyb: n = 9; WT: n = 10): reduced total B cells, B2- and FO B cells ($p < 0.001$), and increased $CD3^+$ and $CD4^+$ T-cell representation ($p < 0.01$ and $p < 0.05$, respectively; GE × CE interaction, $p < 0.0001$). (e) Spleen (Dp1Tyb: n = 10; WT: n = 13): reduced total B-cell, B2- and FO B-cell representation ($p < 0.001$), and increased $CD3^+$ ($p < 0.001$) and $CD4^+$ T-cell representation ($p < 0.01$; GE ×

CE interaction, $p < 0.0001$). (f) The mLN (Dp1Tyb: n = 10; WT: n = 13): reduced total B-cell, B2- and FO B-cell representation ($p < 0.05$), and increased $CD3^+$ ($p < 0.05$) and $CD4^+$ T-cell representation ($p < 0.001$; GE × CE interaction, $p < 0.001$). For each tissue, equal numbers of viable cells, normalized to the number of viable cells recovered from that tissue, were exported. Cell frequencies are expressed as the percentage of $CD45^+$ cells within each tissue; plasma-cell frequencies are expressed as the percentage of total live cells. For each tissue, data were analyzed by two-way mixed ANOVA with genotype and cell type as factors, and mouse ID as a random effect, followed by FDR-adjusted post hoc comparisons. Data are presented as mean ± SD. Each point represents an individual mouse. GE, genotype effect; CE, cell-type effect. Statistical significance is denoted as * $p < 0.05$, ** $p < 0.01$, *** $p < 0.001$, and **** $p < 0.0001$.

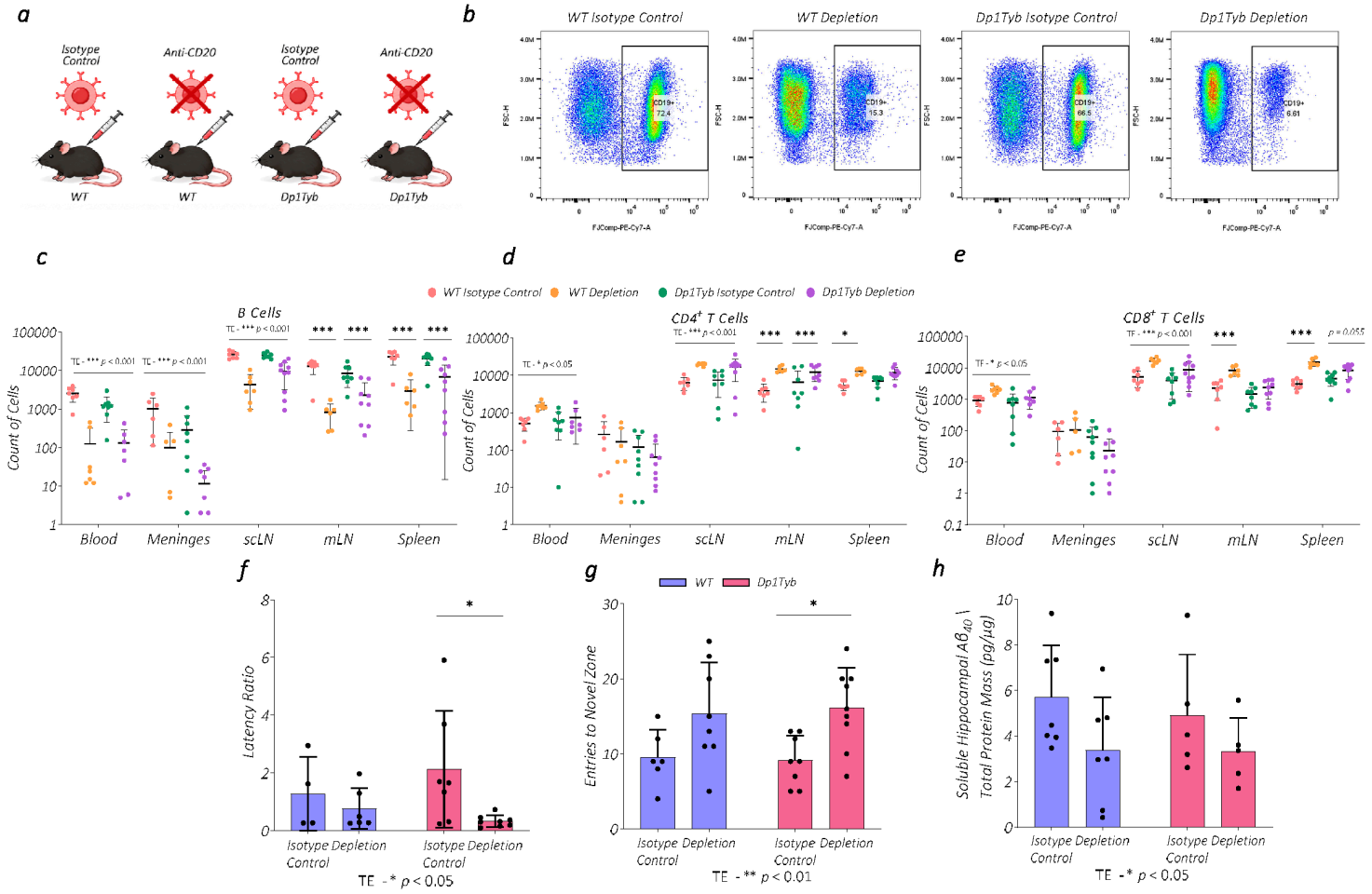


Figure 4

B-cell depletion increases peripheral T-cell abundance, improves short-term memory, and reduces hippocampal $mA\beta_{40}$. (a) B-cell depletion experimental design. Aged male Dp1Tyb and WT mice received intraperitoneal anti-CD20 antibody (150 µg/mouse) or an isotype-matched control every three weeks for four months, generating four groups: WT isotype control, WT depletion, Dp1Tyb isotype control, and Dp1Tyb depletion. Schematic illustration prepared with OpenAI ChatGPT. (b) Representative flow

cytometry demonstrating efficient $CD19^+$ B-cell depletion in Dp1Tyb and WT mice following anti-CD20 treatment compared with isotype controls. (c-e) Absolute immune-cell counts across blood, meninges, scLN, mLN, and spleen. For each tissue, equal numbers of viable cells, normalized to the number of viable cells recovered from that tissue, were exported (Dp1Tyb isotype control: n = 8-9; Dp1Tyb depletion: n = 7-10; WT isotype control: n = 6-7; WT depletion: n = 6-7). **(c)** Anti-CD20 treatment markedly reduced $CD19^+$ $B220^+$ B-cell abundance across the examined tissues. Significant treatment effects were detected in blood, meninges, and scLN (TE, $p < 0.001$), while post hoc comparisons demonstrated significant reductions in both genotypes in mLN and spleen ($p < 0.001$). **(d)** B-cell depletion increased $CD4^+$ T cells in the blood (TE, $p < 0.05$) and in the scLN (TE, $p < 0.001$), with no significant differences in the meninges. In the mLN, $CD4^+$ T-cell abundance was significantly increased in both Dp1Tyb and WT mice ($p < 0.001$). In the spleen, anti-CD20 treatment significantly increased $CD4^+$ T-cell abundance in WT mice ($p < 0.05$), whereas a similar non-significant increase was observed in Dp1Tyb mice. **(e)** $CD8^+$ T-cell abundance was similarly affected by B-cell depletion in a tissue- and genotype-dependent manner. In the blood, a significant overall treatment effect was detected for increased $CD8^+$ T-cell abundance (TE, $p < 0.05$). No significant differences were detected in the meninges. In the scLN, anti-CD20 treatment produced an overall treatment effect (TE, $p < 0.001$). In the mLN, $CD8^+$ T-cell abundance was significantly increased following anti-CD20 treatment in WT mice ($p < 0.001$), whereas no changes were detected in Dp1Tyb mice. In the spleen, $CD8^+$ T-cell abundance was significantly increased in WT mice ($p < 0.001$), while Dp1Tyb mice showed a similar trend ($p = 0.055$). Three-way mixed ANOVA with genotype, treatment, and cell type as factors, and mouse ID as a random effect, followed by FDR-adjusted post hoc comparisons. Data are displayed on a $\log_{10}$ scale. (f) Y-maze forced-choice. B-cell depletion significantly reduced the latency ratio (novel-arm latency relative to familiar-arm latency) (TE, $p < 0.05$), with a significant reduction in Dp1Tyb mice in post hoc analysis ($p < 0.05$). (g) OLR. B-cell depletion increased entries into the novel-object location zone (TE, $p < 0.01$), with a significant increase in Dp1Tyb mice in post hoc analysis ($p < 0.05$). For f-g: (Dp1Tyb isotype control: n = 8; Dp1Tyb depletion: n = 9; WT isotype control: n = 6; WT depletion: n = 8). (h) B-cell depletion reduced soluble hippocampal $mA\beta_{40}$ across genotypes (TE, $p < 0.05$) (Dp1Tyb isotype control: n = 5; Dp1Tyb depletion: n = 5; WT isotype control: n = 7; WT depletion: n = 7). For f-h: Two-way ANOVA with genotype and treatment as factors, followed by Tukey's post hoc test. Data are presented as mean ± SD. Each point represents an individual mouse. TE, treatment effect. Statistical significance is denoted as * $p < 0.05$, ** $p < 0.01$, *** $p < 0.001$, and **** $p < 0.0001$.

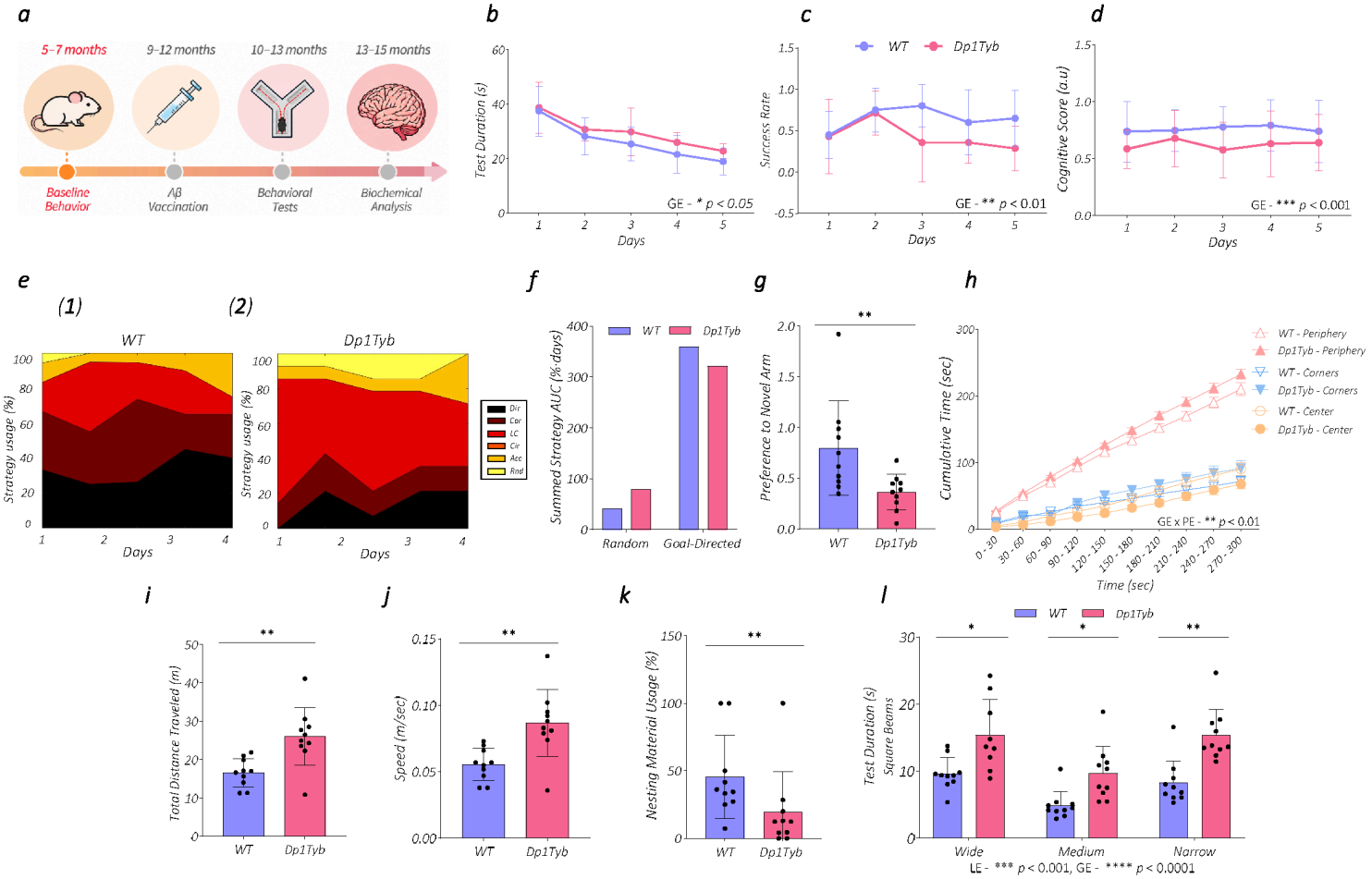


Figure 5

Middle-aged (5-7-month-old) female Dp1Tyb mice exhibit impaired cognition, hyperactivity, reduced nesting, and motor deficits. (a) Study timeline for the vaccination experiment. Baseline behavioral testing was performed at 5-7 months of age, followed by vaccination at 9-12 months, post-vaccination behavioral testing at 10-13 months, and biochemical analysis at 13-15 months. Schematic illustration prepared with OpenAI ChatGPT. Panels b-l show pre-vaccination baseline behavioral measurements. (b-f) MBM (Dp1Tyb: n = 7; WT: n = 10). (b) Test duration decreased across training days in both genotypes and was significantly greater in Dp1Tyb mice than in WT controls (GE, $p < 0.05$). (c) Success rate was lower in Dp1Tyb mice (GE, $p < 0.01$). (d) Cognitive score, which weights search strategies according to their spatial efficiency, was reduced in Dp1Tyb mice (GE, $p < 0.001$). (e) Search-strategy composition across training days is shown for (e_1) WT and (e_2) Dp1Tyb mice. (f) Summed AUC of random and goal-directed strategies demonstrates lower cumulative use of efficient, goal-directed strategies in Dp1Tyb mice. Two-way repeated-measures ANOVA with genotype and training day as factors, followed by Šídák's post hoc test. (g) Y-maze forced-choice (n = 10 per group). Dp1Tyb mice showed lower novel-arm preference than WT mice ($p < 0.01$). Normality was assessed using the Shapiro-Wilk test, followed by a Mann-Whitney test. (h-j) OFA (n = 10 per group). (h) Cumulative regional occupancy across the 5 min

session revealed a significant GE × PE effect ($p < 0.01$). (i) Dp1Tyb mice traveled a greater total distance ($p < 0.01$) and (j) moved at a higher average speed ($p < 0.01$). Two-way repeated-measures ANOVA with genotype and test phase as factors, followed by Šídák's post hoc test. (k) Nesting (n = 10 per group). Dp1Tyb mice used a smaller proportion of the provided nesting material than WT mice ($p < 0.01$). (l) Beam-walking (n = 10 per group). Female Dp1Tyb mice required longer traversal times across wide, medium, and narrow square beams, with significant LE and GE effects ($p < 0.001$ and $p < 0.0001$, respectively). Post hoc analysis revealed elevated test duration in Dp1Tyb mice across all three beam widths ($p < 0.05$ to $p < 0.01$). Two-way repeated-measures ANOVA with genotype and beam width as factors, followed by Šídák's post hoc test. Data are presented as mean ± SD. Each point represents an individual mouse. GE, genotype effect. LE, level effect. PE, phase effect. Statistical significance is denoted as * $p < 0.05$, ** $p < 0.01$, *** $p < 0.001$, and **** $p < 0.0001$.

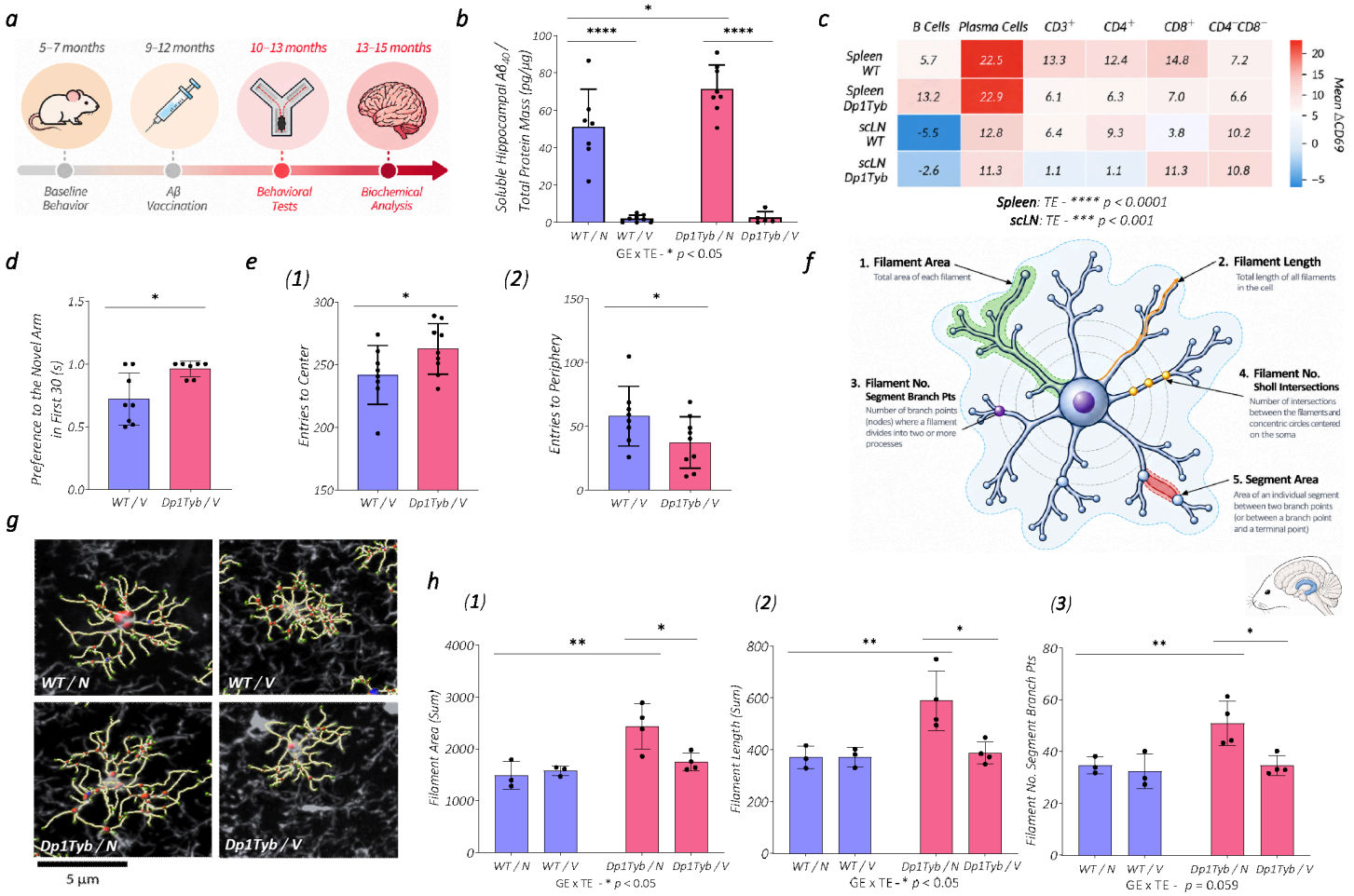


Figure 6

mAβ immunization improves short-term memory and anxiety-like behavior, reduces mAβ_{40} levels, and partially restores hippocampal microglial morphology. (**a**) **Study timeline for the vaccination experiment**. Schematic illustration prepared with OpenAI ChatGPT. (**b**) mAβ_{40} was quantified in naïve WT

(WT/N), vaccinated WT (WT/V), naïve Dp1Tyb (Dp1Tyb/N), and vaccinated Dp1Tyb (Dp1Tyb/V) mice. **Soluble hippocampal mAβ_{40} levels showed a significant GE × TE interaction ($p < 0.05$). Post hoc analysis revealed significantly lower soluble mAβ_{40} levels in vaccinated compared with naïve mice within both genotypes ($p < 0.0001$).** Dp1Tyb/N **mice also exhibited significantly higher soluble mAβ_{40} levels than** WT/N **mice ($p < 0.05$; Dp1Tyb/N: $n = 8$; Dp1Tyb/V: $n = 5$; WT/N: $n = 7$; WT/V: $n = 8$).** (**c**) Antigen-responsive lymphocyte activation following ex vivo mAβ stimulation was assessed by the frequency of surface $CD69^+$ cells in the spleen and scLN. For each mouse, ΔCD69 was calculated as the stimulated $CD69^+$ (mAβ stimulation) frequency minus the unstimulated $CD69^+$ frequency. Positive values indicate increased $CD69^+$ expression following mAβ stimulation, whereas negative values indicate decreased $CD69^+$ expression. Heatmap values show the mean ΔCD69 for each immune-cell population and genotype. (TE, $p < 0.0001$ for spleen; TE, $p < 0.001$ for scLN; Dp1Tyb/V: n = 4-5; WT/V: n = 2-5). Statistical analysis was performed on the original $CD69^+$ frequencies using three-way mixed ANOVA with genotype, cell type, and treatment as factors, and mouse ID as a random effect, followed by FDR-adjusted post hoc comparisons. For each tissue, equal numbers of viable cells, normalized to the number of viable cells recovered from that tissue, were exported. Cell frequencies are expressed as percentages of $CD45^+$ cells within each tissue; plasma-cell frequencies are expressed as percentages of total live cells. Heatmap visualization prepared with OpenAI ChatGPT. (**d**) **T-maze** (Dp1Tyb/V: n = 9; WT/V: n = 8). During the first 30 s of the test, Dp1Tyb/V mice showed greater preference for the novel arm than WT/V mice ($p < 0.05$). Normality was assessed using the Shapiro-Wilk test followed by the Mann-Whitney test. (**e**) **OFA** (Dp1Tyb/V: n = 9; WT/V: n = 8). Dp1Tyb/V mice made (**e_1**) fewer entries into the periphery ($p < 0.05$) and (**e_2**) more entries into the center ($p < 0.05$) than WT/V mice. Normality was assessed using the Shapiro-Wilk test followed by an unpaired t-test. (**f**) Schematic of microglial morphometric features quantified using Iba1-labeled tissue and Imaris Filament Tracer, including filament area, total filament length, branch-point-related measures, Sholl intersections, and segment area. (**g**) Representative $Iba1^+$ hippocampal microglia and filament reconstructions from WT/N, WT/V, Dp1Tyb/N, and Dp1Tyb/V mice, scale bar: 5 µm. **(h)** Quantitative analysis of hippocampal microglial morphology (Dp1Tyb/N: n = 4; Dp1Tyb/V: n = 4; WT/N: n = 3; WT/V: n = 3). **(h_1)** Filament area showed a significant GE × TE interaction ($p < 0.05$). Post hoc analysis revealed significantly elevated filament area in Dp1Tyb/N mice compared with WT/N mice ($p < 0.01$), while vaccination significantly reduced filament area in Dp1Tyb mice ($p < 0.05$). **(h_2)** Filament length showed a significant GE × TE interaction ($p < 0.05$). Post hoc analysis revealed significantly greater filament length in Dp1Tyb/N mice compared with WT/N mice ($p < 0.01$), while vaccination significantly reduced filament length in Dp1Tyb mice ($p < 0.05$). **(h_3)** The number of segment branch points showed a non-significant trend toward a GE × TE interaction ($p = 0.059$). Post hoc analysis revealed significantly more segment branch points in Dp1Tyb/N mice compared with WT/N mice ($p < 0.01$), while vaccination significantly reduced the number of segment branch points in Dp1Tyb mice ($p < 0.05$). **For b and h**: Two-way ANOVA with genotype and treatment as factors, followed by Tukey's post hoc test. Data are presented as mean ± SD. Each point represents an individual mouse. TE, treatment effect. GE, genotype effect. Statistical significance is denoted as * $p < 0.05$, ** $p < 0.01$, *** $p < 0.001$, and **** $p < 0.0001$.

Supplementary Files

This is a list of supplementary files associated with this preprint. Click to download.

- SupplementaryFilesOkun.docx